# Defect Dynamics in Amorphous Colloidal Monolayers under Shear

#### A Thesis

submitted to

Indian Institute of Science Education and Research Pune
in partial fulfillment of the requirements for the

BS-MS Dual Degree Programme

by

Rhuthwik S



Indian Institute of Science Education and Research Pune Dr. Homi Bhabha Road, Pashan, Pune 411008, INDIA.

April, 2023

Supervisor: Dr. Vijayakumar Chikkadi

© Rhuthwik S 2023

All rights reserved

## Certificate

This is to certify that this dissertation entitled "Defect Dynamics in Amorphous Colloidal Monolayers under Shear" towards the partial fulfilment of the BS-MS dual degree programme at the Indian Institute of Science Education and Research, Pune represents study/work carried out by Rhuthwik S at Indian Institute of Science Education and Research under the supervision of Dr. Vijayakumar Chikkadi, Assistant Professor, Department of Physics during the academic year 2022-2023.

N. L. O. UK.

Dr. Vijayakumar Chikkadi

#### Committee:

Dr. Vijayakumar Chikkadi

Dr. G.V. Pavan Kumar



## **Declaration**

I hereby declare that the matter embodied in the report entitled Defect Dynamics in Amorphous Colloidal Monolayers under Shear are the results of the work carried out by me in collaboration with Ratimanasee Sahu at the Department of Physics, Indian Institute of Science Education and Research, Pune, under the supervision of Dr. Vijayakumar Chikkadi and the same has not been submitted elsewhere for any other degree.

Rhuthwik S

Rhuthwik Skanda

# Acknowledgments

I am deeply grateful to everyone who has supported and contributed to the successful completion of my Master's thesis in experimental physics at IISER Pune. I would like to express my heartfelt appreciation to my thesis advisor, Professor Vijayakumar Chikkadi, for their invaluable guidance, expertise, and unwavering support throughout my research journey. Their mentorship and encouragement have shaped my understanding of experimental physics and developed my research skills. I am also grateful to Professor Umakant D Rapol, and Professor G.V. Pavan Kumar, for their support throughout the academic journey at IISER. I am grateful to my fellow lab mates at the Soft-matter lab and AMO Lab for their insights, feedback, and technical assistance, which have enriched my research and improved the quality of my work.

I would like to extend my gratitude to the technical and engineering staff at IISER Pune for their assistance with laboratory setup and equipment maintenance, as well as to my family and friends for their unwavering support and motivation. Lastly, I am thankful to the funding agencies and grants that have provided financial support for my research, enabling me to conduct experiments and analyze results. In conclusion, I am immensely grateful to everyone who has contributed to my Master's thesis in experimental physics, and their support and encouragement have been indispensable to my academic success.



## Abstract

Studying amorphous/disordered solids is challenging compared to their ordered counterparts, crystals [1, 2]. Lattice imperfections or defects in crystals are known to play a significant role in deformation, as the defects within crystals begin to move when an external load is applied, resulting in permanent deformation or plasticity. These defects are referred to as plasticity carriers. However, amorphous materials lack a reference lattice to identify defects. In this study, we use optical tweezers and dense colloidal suspensions to investigate the relationship between plastic activity and microscopic structure in amorphous substances.

Shear fields in a colloidal monolayer are generated using a holographic optical trap with Laguerre Gaussian beam and a spatial light modulator. With this setup, we examine the relationships between defect dynamics and microstructure in a quasi-2D system of colloidal glasses, including the orientation of defects with respect to the shear direction. We have built the instrumentation of time-shared optical traps to investigate the effect of random pinning on phonon modes in colloidal crystals and glasses.

# Contents

A	bstra	act	xi
1	Intr	roduction	1
	1.1	Amorphous solids under Shear	3
	1.2	Theoretical Models of Deformation	4
	1.3	Objective of the thesis	8
	1.4	Overview of the thesis	8
2	Opt	ics	11
	2.1	Fourier Optics	11
	2.2	Electromagnetic Theory of light	20
	2.3	Optical Tweezer	32
	2.4	Radiation Pressure	32
	2.5	Optical trapping in Geometric optics region	33
	2.6	Optical trapping in Rayleigh regime	34
	2.7	Holographic Optical Tweezers	34
3	Exp	perimental Details	37
	3.1	Colloids and Brownian motion	37

5	Con	nclusion	65
4	Res	ults and Discussion	55
	3.5	MSD Mean Square Displacement:	48
	3.4	Time Shared Optical Traps	42
	3.3	Holographic Optical Tweezer	39
	3.2	Making of sample wells using Photolithography and making dense colloidal amorphous solid	38

# Chapter 1

## Introduction

Amorphous Solid materials do not have long-range order and are disordered structurally. Many of the day-to-day materials are amorphous solids and they have a wide range of applications in various fields like pharmaceuticals, the food processing industry, cosmetics, electronics, etc. Understanding of mechanical behaviour of these amorphous solids is beneficial in modelling earthquakes and making stronger materials. The study of amorphous solids under external forces like shear is used to understand the interesting phenomenon of the mechanical behaviour of amorphous solids.

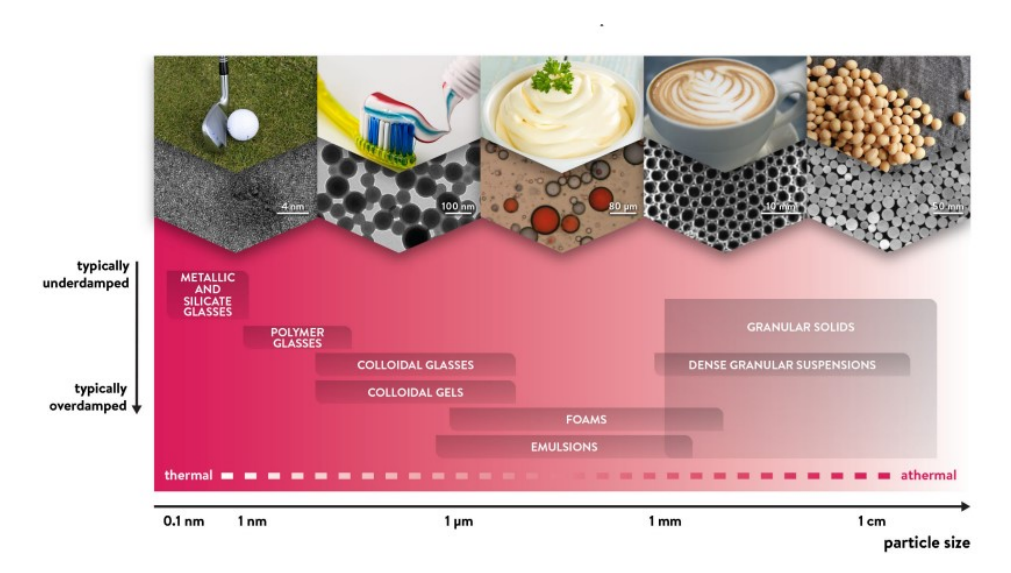


Figure 1.1: The figure classifies a different range of amorphous materials based on their elementary particles' size and damping regime.[3]

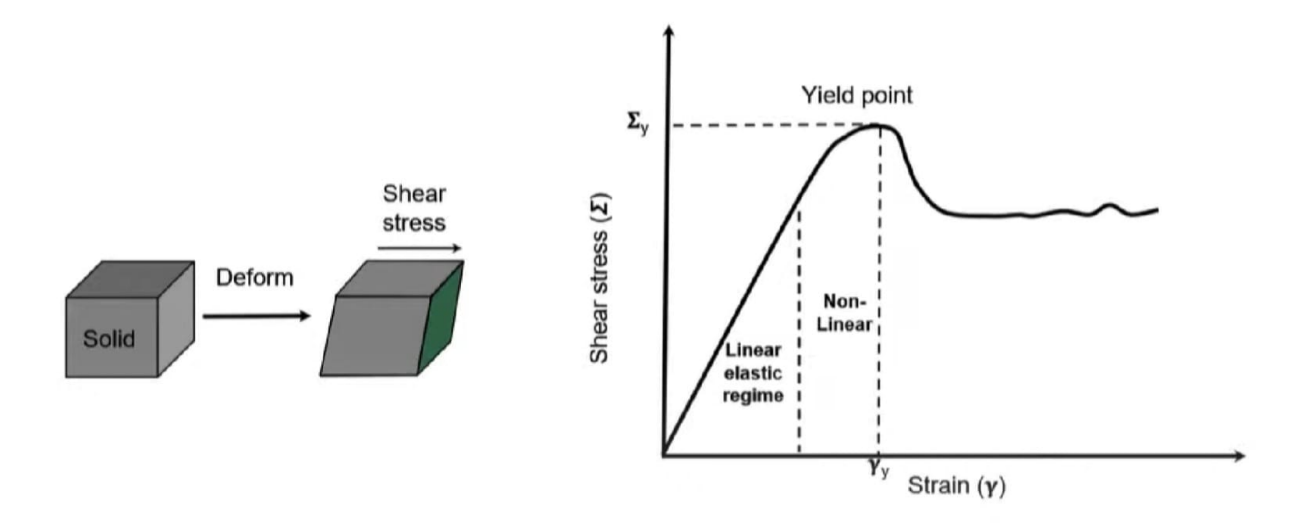


Figure 1.2: shear stress versus strain on a solid material when we apply shear stress

Particles in the solid material interact with each other through various intermolecular forces. When shear stress is applied to the material, these particles start to slide past each other and this results in the deformation of the material. At small strains, the behaviour of the material is linearly elastic, meaning that the deformation is directly proportional to the applied stress. This is because the particles are able to slide past each other without causing any permanent deformation. However, as the applied stress increases, the deformation becomes non-linear and the material exhibits plastic deformation. At a certain point, known as the yield point, the material either fails if it is brittle or starts to flow if it is ductile. This is because the applied stress is now sufficient to cause permanent deformation of the material, and the intermolecular forces between the particles can no longer hold the material together. To understand this behaviour at the macroscopic level, we need to look at the interactions between the colloidal particles in the material. These particles are held together by various intermolecular forces such as van der Waals forces, hydrogen bonding, and electrostatic interactions. When shear stress is applied to the material, these forces are disrupted, and the particles start to slide past each other. As the applied stress increases, the particles start to deform and rearrange themselves, leading to the non-linear behaviour of the material. At the yield point, the deformation becomes permanent, and the material either fails or starts to flow depending on its properties. Under shear stress, the behaviour of solid materials is determined by the interactions between the colloidal particles in the material.

Understanding this behaviour at a microscopic level is essential for designing materials with specific properties and for predicting their mechanical behaviour under different conditions.

When Mechanical stress like shear is applied to a crystalline solid which has a longrange order the imperfection in lattice arrangement or defects play a significant role in the deformation but in the case of amorphous solids, there will be complex rearrangements of particles leading to the substantial difference in their mechanical properties.

In crystal when stress is applied defects will play a major role and act as plasticity carriers. As the Roel Dullens' Oxford colloidal group performed the experiment on colloidal crystals and holographic optical tweezers to generate grain boundary loops[1]. These defects of grain boundary loops will shrink when shear from the holographic optical tweezers is removed. So the main inspiration of this thesis comes from the idea that these ideas can also be applied to amorphous solids by applying shear with holographic optical tweezers and generating defects in the system and identifying its positions and studying its dynamics. We find stress in amorphous solids and identify these features in amorphous solids.

## 1.1 Amorphous solids under Shear

When under external stress an amorphous material may exhibit macroscopic flow. Even though this movement can be uniform throughout the material, it frequently localizes, which causes instability and failure in the long run. Despite the long-known prevalence of flow instabilities in geology, as demonstrated by landslides, shear banding[4] is a common event that happens in a wide variety of amorphous materials. Shear striping is seen in amorphous materials such as molecular glasses, solutions, foams, and emulsions [5]. Due to thermally induced relaxation processes, molecular glasses in particular show uniform flow under tiny applied strains [6]. These relaxation processes, however, cannot proceed fast enough to maintain the applied shear rate when there are significant applied pressures. The glass consequently divides into bands that move at various shear rates. Despite this knowledge, the process causing the development of these rings is still unclear.

Glass is a unique state of matter that exhibits properties of both liquids and solids. It is formed by rapidly cooling a liquid, which results in an increase in viscosity and a transition to a metastable state. This transition is known as the glass transition, and it is considered the most significant unsolved problem in condensed matter physics. Due to the large relaxation timescales associated with glass, many materials are considered glassy, including densely packed colloidal particles, emulsions, foams, granular materials, proteins, and more. These materials exhibit some degree of glassy dynamics and have their own phase diagrams. In the metastable state, the particles remain caged by their neighbors, and the structure remain frozen, similar to a crystalline substance. The relaxation time diverges at the glass transition point, and the system is no longer ergodic on experimental timescales.

### 1.2 Theoretical Models of Deformation

#### Eyring's model

When Particles are rearranged, a shear transformation occurs. The positions of the particles before the rearrangement and after the rearrangement are considered to be relative stability positions, which means they are in a local minimum of free energy. Under normal circumstances, with external force zero, Thermal fluctuations will provide the activation energy for the transition from one minimum to another minimum, and particle jumps in all directions are likely to occur equally. However, when an external force is non-zero, in the direction of the force the energy barrier will be reduced. As a result, rearrangements of particles are biased towards the direction of the force applied, resulting in a flow. The right side of Figure 1.3 (a) and (b) shows the energy barrier when shear stress is applied and shear stress is not applied.  $\tau$ . The Deformation rate based on the transition is

$$\dot{\gamma} = \Delta \epsilon_0 (r_+ - r_-) \tag{1.1}$$

here  $\epsilon_0$  is strain resulting from transformation and  $r_+$  and  $r_-$  are forward moves rate and backward moves rate respectively. The forward moves rate and backward moves rate when externally applied stress  $\sigma$  are given by

$$r_{\pm} = \omega_0 e^{[(-E_0 \pm \sigma\Omega_0)/kT]} \tag{1.2}$$

where,  $\Omega_0$  is the activation volume and  $\omega_0$  is a microscopic attempt frequency, usually of the order of 5-10 particles. So we can write the deformation rate equation as [7].



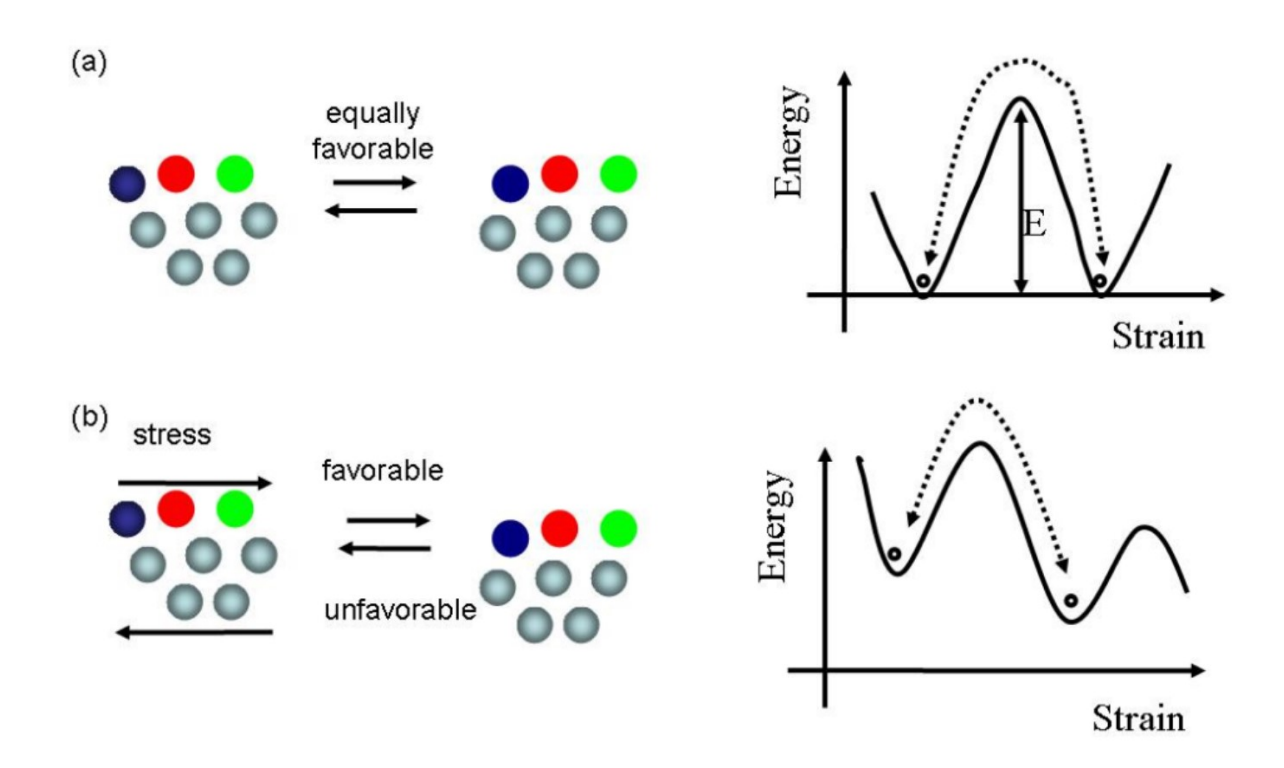


Figure 1.3: Erying's model. The particle rearrangement and the energy barrier in the shear are non-zero (a) and the shear is zero d(b).[8]

#### Spaepen's model

A key component of the formulation mentioned above is the free volume distribution, which represents the available volume for an individual particle to displace without disrupting surrounding particles. In areas with a large amount of free volume, shear transformations are more likely to initiate because of the weak coupling to the surrounding area. The likelihood of particle rearrangement increases with increasing free volume. In Spaepen's free volume model [9], the rate of deformation is described by the following equation:

$$\dot{\gamma} = \Delta f e^{\left(-\frac{\epsilon_0 v^*}{v_f}\right)} e^{\left(-\frac{E_0}{KT}\right)} \sinh\left(\frac{\Omega_0 \tau}{KT}\right) \tag{1.4}$$

where  $\Delta f$  is the proportion of the sample which can be undergoing deformation,  $v^*$  is the volume of the particle, and  $v_f$  is the average free volume available to the particle. The term  $\Delta f e^{\left(-\frac{\epsilon_0 v^*}{v_f}\right)}$  in equation 1.4, estimates the proportion of sites which can potentially undergo a transformation based on the distribution of free volume in the given system.

#### Argon's model

Shear transformation zones are suggested to be inclusions that are elastically linked to the surrounding medium of material as proposed by Argon[6]. This was a significant advancement over models which were discussed earlier, which assumed that shear transformations occurred as independent events within the Eyring model. Argon's hypothesis suggested that a flip would occur when a zone deformed elastically up to a certain critical level of strain, ranging from approximately 2-4% [7, 10], causing it to become unstable. As mentioned by Eshelby [11, 12], this type of shear transformation results in increases in strain  $\Delta \epsilon_0$  and elastic strain energy  $\Delta \epsilon$  in a spherical region of size  $\Omega_0$ .

$$\Delta \epsilon = \frac{7 - 5v}{30(1 - v)} \mu \Delta \epsilon_0^2 \Omega_0 \tag{1.5}$$

where  $\mu$  is the shear modulus. So the rate of deformation for this model is

$$\dot{\gamma} = 2\omega_0 \Delta \epsilon_0 e^{\left(-\frac{\Delta \epsilon + E_0}{KT}\right)} \sinh\left(\frac{\Omega_0 \tau}{KT}\right) \tag{1.6}$$

#### **Shear Localization**

Models put forth by Spaepen and Argon attempt to explain why shear transformation zones begin to develop in regions with higher free volumes at lower stress levels. To generate free volume and cause local dilation, a particle may force nearby particles under conditions of greater stress. The surrounding particles are diffused and the excess free volume is eliminated by a competitive relaxation process. The sheared areas may keep a significant quantity of free volume if the formation of free volume is quick and the annihilation is gradual, which will cause localized softening. It has been proposed that these disturbances lead to shear

bands in the system.

#### Soft glassy rheology - mesoscopic model (P.Sollich)

It is a mesoscopic model we treat small regions instead of particles. These regions are associated with a strain variable l and some yield threshold. If strain exceeds the threshold then particles rearrange and relax. and each zone had elastic energy E characteristic local yield. The dynamics of the microscopic yield is described by the Probability distribution p(l, E, t)

$$\frac{\partial}{\partial t}P = -\dot{\gamma}\frac{\partial}{\partial t}P - \Gamma_0 e^{-(E - \frac{1}{2}kl^2)/x}P + \Gamma(t)\rho(E)\delta(l)$$

The first term is the Elastic loading between successive yield events, the second term is the yielding of the mesoscopic region and the third term is the relaxation of regions to the new equilibrium. here we considered that if a region is flipping it doesn't affect other regions.[13]

#### Elasto-Plastic Model

This is also a mesoscopic model[3] that describes the evolution of elasto-plastic elements on a regular square lattice. Each lattice point is associated with yield stress. when the external stress is applied each of these lattice points is associated with a certain threshold value, if exceeds the local threshold value it will fail and redistribute its stress but redistribution is anisotropic

 $n(r,t)=0\longrightarrow 1$  if  $\sigma>\sigma_y$  where  $sigma_y$  is threshold stress drawn from distribution

$$n(r,t) = 0 \longleftarrow 1 \text{ when } \int dt' |\partial_t \sigma(t')/\mu + \dot{\gamma_j}^{pl}(t')| \ge \gamma_c$$

Where n = 0 is where block is completely elastic and n = 1 if not.

elastoplasticity models (EPM), which are coarse-grained models used for modeling plasticity in amorphous substances. In the simplest flow scenario, the material is divided into mesoscopic units and loaded elastically till they hit a yield threshold condition and turn plastic. Following the end of the plastic event, the blocks regain their elastic properties once the stress has been dispersed to other units via an elastic stress field. The default elastic response, the local yield criteria, the stress redistribution during plasticity, and the recovery

criterion are the four preset rules on which EPMs are built. Utilizing equations of evolution for stress carried by each block, contributions from externally imposed shear, nonlocal plastic events, and local relaxation are included in the implementation of these principles. Due to the EPMs' simplicity and generality, several phenomenological models can develop.

$$\frac{\partial \sigma_i}{\partial t} = \mu \dot{\gamma} + \mu \sum_j G_{ij} \frac{\partial \dot{\gamma_j}^{pl}}{\partial t}$$

$$\frac{\partial \dot{\gamma_j}^{pl}}{\partial t} = n_j \frac{\sigma_j}{\mu \tau}$$

where the first part of the equation is the elastic part with an applied shear rate,  $G_{ij}$  is the stress kernel (self and neighbour) and  $\frac{\partial \dot{\gamma}_j^{pl}}{\partial t}$  is the plastic part

## 1.3 Objective of the thesis

The Objective of the thesis is to understand the amorphous system under Shear using holographic optical tweezers to understand how amorphous system particles undergo rearrangements under shear stress. We also discuss on the instrumentation of time-shared optical tweezers to study how random pinning of the colloidal particles will effect the phonon mode in the system. In this project, we develop a robust Holographic optical tweezers setup and time-shared optical tweezers setup. This involves the Generation of LG Beam which is the major factor in our system. Once the system is ready we take shared data of colloidal monolayer and understand the different parameters to understand the defects dynamics and orientation of defects with respect to shear direction.

### 1.4 Overview of the thesis

**Chapter 1** discusses theoretical models for the deformation of amorphous solids, such as Eyring's model, Argon's model, Spaepen's model, and mean-field models like the Elasto-Plastic model.

Chapter 2 provides a basic understanding of Fourier optics, including Fresnel diffraction, Angular Spectrum Analysis, and Lens 1F System - Lens Fourier Transforms. These concepts are used to comprehend Holographic Optical Tweezers. The chapter also covers the electromagnetic theory of light and how light (optical vortex) can be used to shear a system. Additionally, the basic principles of optical tweezers are discussed, including how to understand them in different regions such as the Geometric optics region and Rayleigh regime. Holographic optical tweezers and the Gerchberg-Saxton (GS) algorithm to generate LG Beam are also discussed in this chapter.

Chapter 3 focuses on experimental details such as creating sample cells using photolithography, making colloidal amorphous monolayers, setting up optical circuits for Holographic optical tweezers and time-shared optical traps, and generating LG Beam and time-shared optical traps. The chapter also covers how to drive AOD from RF synthesizer and discusses some of the parameters used to analyze the data, such as  $D_{min}^2$ , MSD, Radial Distribution function, Voronoi tessellation, and Delaunay triangulation.

Chapter 4 presents the results found from the analysis of sheared 2D amorphous solids, including the identification of the location and orientation of defects with respect to the shear direction.

Chapter 5 summarizes the conclusions and discusses future work.

# Chapter 2

# **Optics**

## 2.1 Fourier Optics

In the area of optics known as Fourier optics, optical data are analysed and manipulated using Fourier transforms. It has many uses in microscopy, holography, spectroscopy, and telecommunications and offers a strong foundation for comprehending how light behaves in different optical systems. Early in the 19th century, Joseph Fourier developed the idea of Fourier optics as a quantitative method for explaining the propagation of light waves. Since that time, Fourier optics has grown in importance as a field of study in optics and photonics, particularly with the advancement of sophisticated optical methods and computers. Any optical system can be viewed as a linear system that reacts to input through a linear operator, which is the fundamental idea behind Fourier optics. Fourier transforms can be used to analyse intricate optical systems because this operator can be expressed as a matrix in the Fourier domain. The evolution of imaging methods, such as confocal microscopy and optical coherence tomography, has been greatly aided by the study of Fourier optics. The Fourier transform spectrometer, Holographic optical tweezers, and Fourier transform holography have both been developed as a result of it. A key idea in wave optics is the Huygens-Fresnel principle, which describes how a waveform moves through a medium. According to this concept, each point on a wavefront produces spherical waves, that can be thought of as the origin of secondary wavelets that travel in all directions. Later, the total waveform is created by adding these wavelets together. The calculation of wave diffraction patterns made possible by this concept is helpful for a number of tasks, including the creation of optical systems like lenses, reflectors, and holograms. Notably, the Huygens-Fresnel principle makes the assumption that waves propagate linearly, which is a reasonable estimate for many optical systems.

#### 2.1.1 Fraunhofer and fresnel diffraction

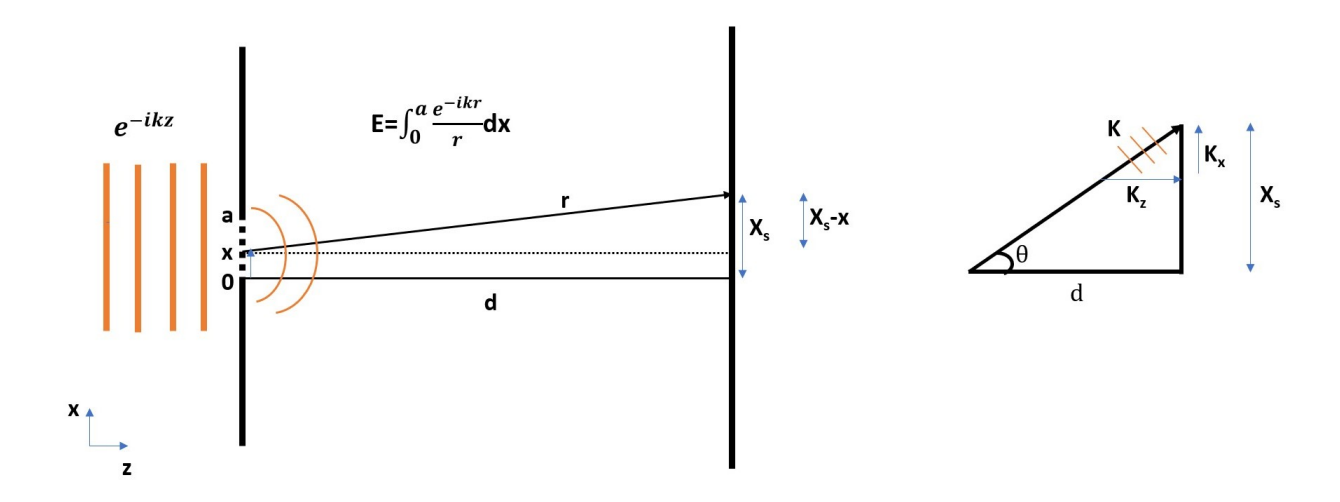


Figure 2.1: Single-Slit Diffraction

In single slit diffraction as shown in figure 2.1, when a plain wave  $e^{-ikz}$  propagating in z-direction incident on a slit of size 'a' then at each point in the slit act as a secondary source producing spherical wavelets. the field of light at a screen at a distance of 'd' from the slit and at a distance ' $X_s$ ' height on the screen will be given by (assume amplitude is 1)

$$E = \int_0^a \frac{e^{ikr}}{r} dx \tag{2.1}$$

so by Pythagoras' theorem and paraxial approximation,

$$r = \sqrt{(X_s - x)^2 + d^2} \tag{2.2}$$

$$r = d\sqrt{1 + \frac{(X_s - x)^2}{d^2}}$$
 (2.3)

$$r = d + \frac{1}{2} \frac{(X_s - x)^2}{d} \tag{2.4}$$

from the right figure 2.1 we can see that  $k_x = ksin\theta = \frac{kX_s}{d}$  and  $\frac{(X_s-x)^2}{d} = \frac{X_s^2-2X_sx+x^2}{d} = \frac{X_s^2-2X_sx}{d}$ , since  $x^2$  is small for Fraunhofer diffraction as  $a << X_s$ ,  $x << X_s$  and  $\theta$  is small

$$g_{out}(X_s) = \int_0^a \frac{e^{ikd} e^{\frac{1}{2}ik\frac{(X_s - x)^2}{d}}}{d + \frac{1}{2}\frac{(X_s - x)^2}{d}} dx \quad \text{(small compare to d)}$$
 (2.5)

$$g_{out}(X_s) = \frac{e^{ikd}}{d} \int_0^a e^{\frac{1}{2}ik\frac{(X_s - x)^2}{d}} dx$$
 (2.6)

$$=A_0 e^{\frac{ikX_s^2}{2d}} \int_0^a e^{\frac{-ikX_sx}{d}} dx \tag{2.7}$$

$$= A_0 C_0 \int_{-\infty}^{\infty} g_{in}(x) e^{-ik_x x} dx \quad g_{in}(x) \text{ is a aperture function}$$
 (2.8)

if  $a \approx X_s$  then we have to use fresnel diffraction

$$g_{out}(X_s) = A_0 \int_0^a e^{\frac{1}{2}ik\frac{(X_s - x)^2}{d}} dx$$
 (2.9)

Convolution:  $f(t) * g(t) = \int_{-\infty}^{\infty} f(\tau)g(t-\tau)d\tau$  Fourier transform will convert convolution to multiplication

$$g_{out}(X_s) = g_{in}(X_s) * e^{\frac{ikX_s^2}{2d}}$$
 (2.10)

$$G_{out}(K_x) = B_0 G_{in}(K_x) \cdot e^{\frac{ikX_s^2}{2d}}$$
 (2.11)

Transform function 
$$H(K_x) = \frac{G_{out}(K_x)}{G_{in}(K_x)} = B_0 e^{\frac{ikX_s^2}{2d}}$$

$$G_{out}(K_x) = H(K_x)G_{in}(K_x)$$
(2.12)

$$g_{out}(K_x) = \mathcal{F}^{-1}(G_{out}(K_x)) \tag{2.13}$$

### 2.1.2 Angular spectrum analysis

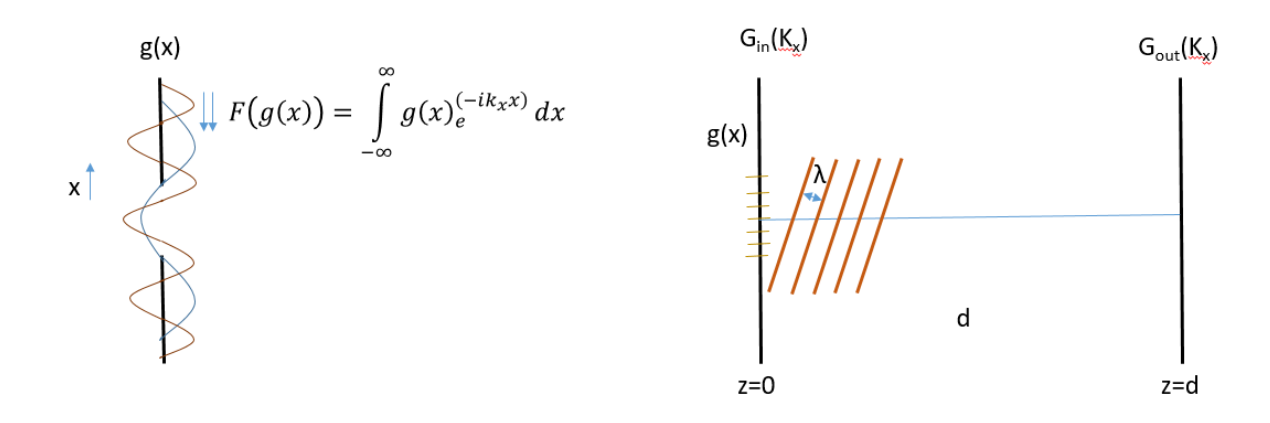


Figure 2.2: Angular spectrum analysis

The study of light waves and their interactions with optical instruments is the focus of the field of Fourier optics, which includes the idea of angular spectrum analysis. Here, a complicated waveform is split down through Fourier transforms to reveal its underlying plane waves. This method offers a practical and effective analytical tool to explain how light waves behave when they travel via space. Any complicated wavefront can be described as a superposition of planar waves with various spatial frequencies and propagation directions, and this is the foundation of the angular spectrum analysis.

The wavefront is first split into a number of narrow segments, every one of which is regarded as a planar wave, in order to perform angular spectrum analysis. The frequency components that emerge from the Fourier transform of each segment are then propagated to the next segment using the free-space propagation equation. Until the complete wavefront is rebuilt in the far field, this procedure is repeated. The benefit of angular spectrum analysis is that it enables highly accurate and effective computation of diffraction patterns and other visual phenomena.

we take the Fourier transform of g(x) function and decompose in terms of plane waves

$$F(g(x)) = \int_{-\infty}^{\infty} g(x)e^{-ik_x x} dx$$
 (2.14)

When an arbitrary plane wave propagates from z=0 to z=d,

$$\vec{K} = \langle K_x, K_z \rangle \tag{2.15}$$

$$= \langle K sin\theta, K cos\theta \rangle \tag{2.16}$$

$$\vec{r} = \langle x, z \rangle \tag{2.17}$$

$$e^{i\mathbf{k}\cdot\mathbf{r}} = e^{i(K_x x + K_z z)} \tag{2.18}$$

(2.19)

the wave at z=0 is given by  $e^{iK_xx}$  and at the distance z=d is  $e^{i(K_xx+K_zd)}$  so the transform function is  $e^{iK_zd}$ 

$$|\vec{K}|^2 = K_x^2 + K_z^2 \tag{2.20}$$

$$K_z^2 = |\vec{K}|^2 - K_x^2 \tag{2.21}$$

$$K_z = K\sqrt{1 - \frac{K_x^2}{K^2}} (2.22)$$

So transform function is given by

$$H_d = e^{iK_z d} (2.23)$$

$$H_d = e^{iKd\sqrt{1 - \frac{K_x^2}{K^2}}} (2.24)$$

$$H_d = e^{iKd} e^{-\frac{iK_x^2 d}{2K}} (2.25)$$

$$H_d = Ce^{-\frac{iK_x^2d}{2K}} \tag{2.26}$$

Therefore we can write the equation

$$G_{out}(K_x) = e^{-\frac{iK_x^2d}{2K}}G_{in}(K_x)$$
 (2.27)

#### 2.1.3 Thin Transparent lens aperture function

when a plane wave propagates in free space for a distance of let's say L the transform function for this plane wave propagation through free space is  $e^{ikL}$  where K is  $2\pi/\lambda$ .

If we have material of refractive index n and the same length L then the plane wave propagates through with a smaller effective wavelength or larger value of K, so the transform function becomes  $e^{iK_0nL}$  where  $K_0$  is  $2\pi/\lambda_0$ ,  $\lambda_0$  free space wavelength.

The Aperture function of refractive index medium is the difference in the phase a plane wave see in medium and the free space. $g_{medium}(x) = e^{i(K_0nL - K_0L)} = e^{i(n-1)K_0L}$ 

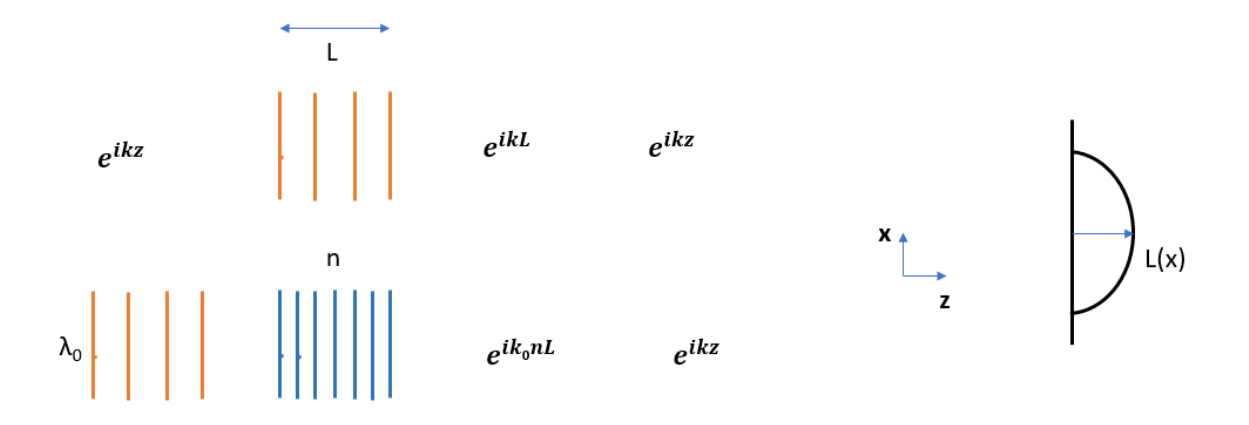


Figure 2.3: lens aperture function

If the plane wave not just propagating towards a constant L, if L is a function of x then the aperture function is  $g_{medium}(x) = e^{i(n-1)K_0L(x)}$ 

For a simple plano-convex spherical lens then

$$x^2 + z^2 = R^2 (2.28)$$

$$x^2 + L(x)^2 = R^2 (2.29)$$

$$L(x) = \sqrt{R^2 - x^2} \tag{2.30}$$

$$L(x) = R\sqrt{1 - \frac{x^2}{R^2}} \tag{2.31}$$

$$L(x) = R - \frac{x^2}{2R}$$
 (Paraxial approximation) (2.32)

aperture function for the lens is

$$g_{lens}(x) = e^{i(n-1)KR}e^{-i(n-1)K\frac{x^2}{2R}}$$
 (constant) (2.33)

$$g_{lens}(x) = Ce^{\frac{-ikx^2}{2f}}$$
 (for Plano convex lens  $\frac{1}{f} = (n-1)\frac{1}{R}$ ) (2.34)

similar arguments can be done for the bi-convex lens. so the transformation of the field through a lens is

$$g_{out} = g_{in}g_{lens} = e^{\frac{-ikx^2}{2f}}g_{in} \tag{2.35}$$

### 2.1.4 Lens 1F System - Lens Fourier Transforms

Consider an input aperture function g(x) at a distance f from the lens at  $x_l$  then the electromagnetic field at a plane  $(X_s)$  at a distance f from the lens is the Fourier transform of the original wave i.e  $g_{out}(X_s) = F(g_{in}(x)) = G_{in}(K_x)$ 

- $G_{lens-}(K_x) = e^{\frac{-iK_x^2f}{2K}}G_{in}(K_x)$  from equation 2.27
- $g_{lens+} = e^{\frac{-ikX_l^2}{2f}}g_{lens-}$  from equation 2.35
- $g_{out}(X_s) = g_{lens+} * e^{\frac{ikX_s^2}{2f}}$  from equation 2.10
- $K_x = \frac{KX_s}{f}$  from fig 2.1

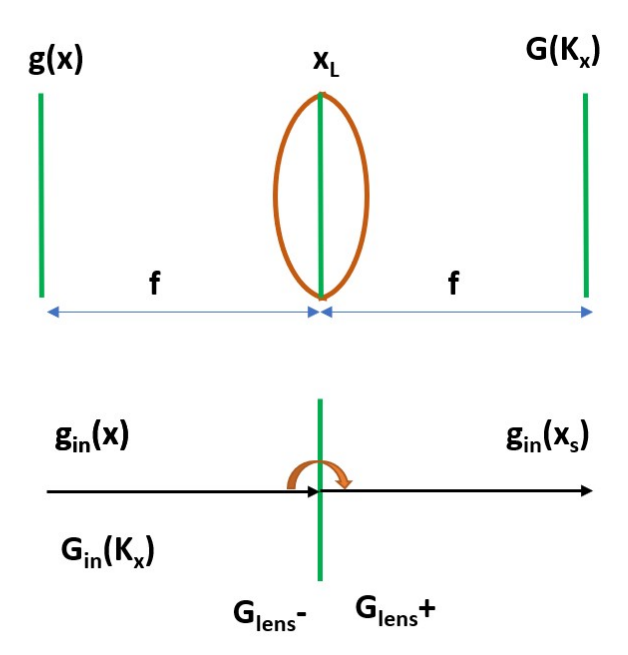


Figure 2.4: Lens 1F System - Lens Fourier Transforms

By using the above equations we can write

$$g_{out}(X_s) = \int_{-\infty}^{\infty} g_{lens+}(x_l) e^{ik\frac{(X_s - x_l)^2}{2f}} dx_L$$
 (2.36)

$$g_{out}(X_s) = e^{\frac{iKX_s^2}{2f}} \int_{-\infty}^{\infty} g_{lens} e^{\frac{iKX_l^2}{2f}} e^{\frac{iKX_sx_l}{f}} dx_L \quad \text{from equation 2.35}$$
 (2.37)

$$g_{out}(X_s) = e^{\frac{iKX_s^2}{2f}} \int_{-\infty}^{\infty} g_{lens} - e^{\frac{-iKx_l^2}{2f}} e^{\frac{iKx_l^2}{2f}} e^{\frac{iKx_sx_l}{f}} dx_L$$

$$(2.38)$$

$$g_{out}(X_s) = e^{\frac{iKX_s^2}{2f}} \int_{-\infty}^{\infty} g_{lens-}e^{iK_xx_l}dx_L$$
 green potion is  $G_{lens-}(K_x) \to F(g_{lens-}(x_l))$  (2.39)

$$g_{out}(X_s) = e^{\frac{iKX_s^2}{2f}}G_{lens-}(K_x)$$
(2.40)

$$g_{out}(X_s) = e^{\frac{iKX_s^2}{2f}} e^{\frac{-iK_x^2}{2K}} G_{in}(K_x)$$
(2.41)

$$g_{out}(X_s) = e^{\frac{iKX_s^2}{2f}} e^{\frac{-iK^2X_s^2f}{2Kf^2}} G_{in}(K_x)$$
(2.42)

$$g_{out}(X_s) = e^{\frac{iKX_s^2}{2f}} e^{\frac{-iKX_s^2}{2f}} G_{in}(K_x)$$
(2.43)

$$g_{out}(X_s) = G_{in}(K_x) \tag{2.44}$$

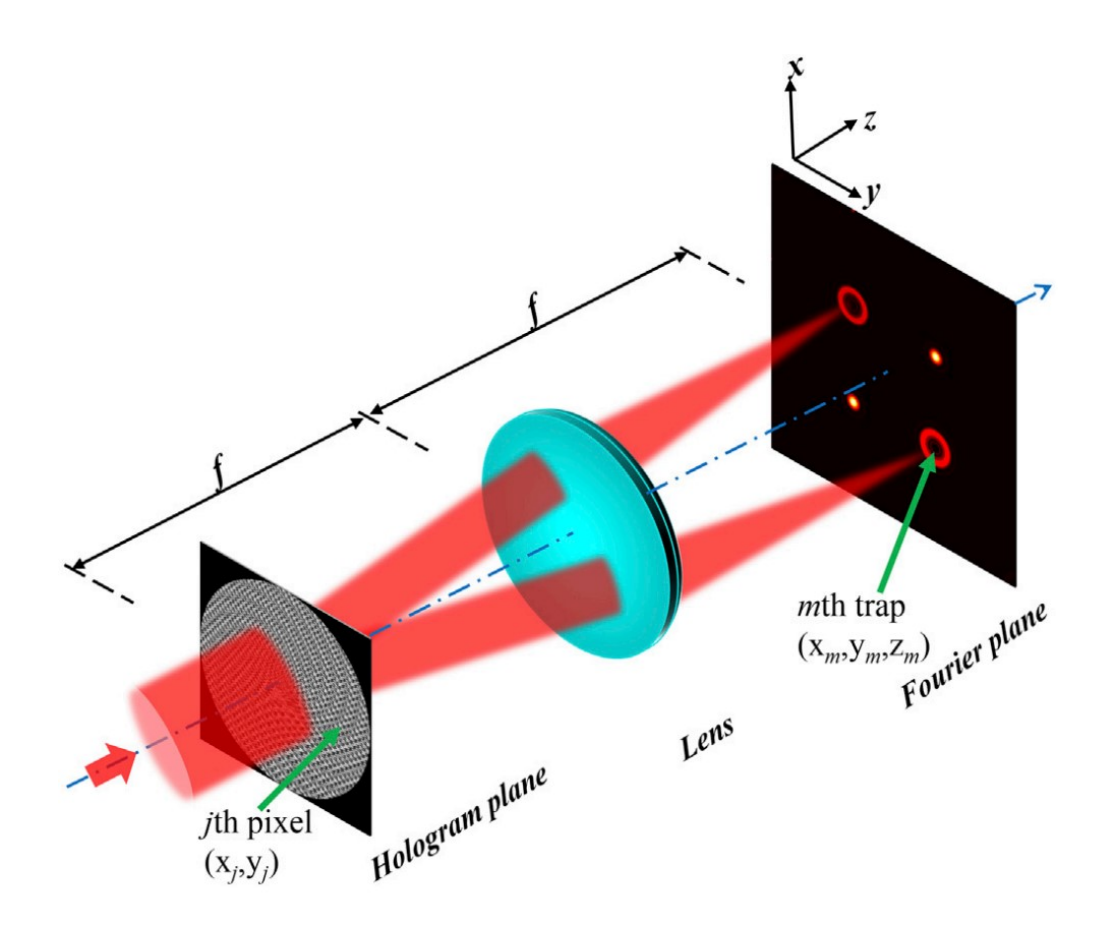


Figure 2.5: Lens 1F System - Lens Fourier Transforms[14]

The hologram and the back aperture of the objective are linked as conjugate image planes, which leads to a direct correspondence between the beam produced by the hologram and the beam in the focal plane. Another important aspect of this relationship is that the complex amplitude of the beam in the trapping plane is essentially the Fourier transform of the beam in the SLM plane.

## 2.2 Electromagnetic Theory of light

The electromagnetic theory of light is a fundamental concept in physics that describes the nature of light as an electromagnetic wave. In the 19th century, James Clerk Maxwell made the initial suggestion, and Heinrich Hertz subsequently verified it experimentally. This theory states that light is a transverse wave that moves through space and is made up of oscillating magnetic and electric fields that are perpendicular to one another and to the direction of transmission. Reflection, refraction, and polarisation are just a few of the events that the electromagnetic theory of light can describe.

Maxwell's equation for the electric and magnetic fields are

$$\nabla . \mathbf{E} = \frac{\rho}{\epsilon_0} \tag{2.45}$$

$$\nabla . \mathbf{B} = 0 \tag{2.46}$$

$$\nabla \times \mathbf{E} = -\frac{\partial \mathbf{B}}{\partial t} \tag{2.47}$$

$$\nabla \times \mathbf{B} = \mu_0 \left( \mathbf{J} + \epsilon_0 \frac{\partial \mathbf{E}}{\partial t} \right) \tag{2.48}$$

### 2.2.1 Electromagnetic waves in Vacuum

In a region of space (vacuum) where there is no charge or current then we can write Maxwell's equation as

$$\nabla . \mathbf{E} = 0 \tag{2.49}$$

$$\nabla . \mathbf{B} = 0 \tag{2.50}$$

$$\nabla \times \mathbf{E} = -\frac{\partial \mathbf{B}}{\partial t} \tag{2.51}$$

$$\nabla \times \mathbf{B} = \mu_0 \epsilon_0 \frac{\partial \mathbf{E}}{\partial t} \tag{2.52}$$

for equations 2.51 and 2.52 find the curl  $(\mathbf{A} \times (\mathbf{B} \times \mathbf{C}) = \mathbf{B}(\mathbf{A}.\mathbf{C}) - \mathbf{C}(\mathbf{A}.\mathbf{B}))$ 

$$\nabla \times (\nabla \times \mathbf{E}) = \nabla(\nabla \cdot \mathbf{E}) - \nabla^2 \mathbf{E} = \nabla \times -\frac{\partial \mathbf{B}}{\partial t} = -\frac{\partial}{\partial t} (\nabla \times \mathbf{B}) = -\mu_0 \epsilon_0 \frac{\partial^2 \mathbf{E}}{\partial^2 t}$$
(2.53)

Similarly

$$\nabla \times (\nabla \times \mathbf{B}) = \nabla(\nabla \cdot \mathbf{B}) - \nabla^2 \mathbf{B} = \nabla \times \left(\mu_0 \epsilon_0 \frac{\partial \mathbf{E}}{\partial t}\right) = \mu_0 \epsilon_0 \frac{\partial}{\partial t} (\nabla \times \mathbf{E}) = -\mu_0 \epsilon_0 \frac{\partial^2 \mathbf{B}}{\partial^2 t} \quad (2.54)$$

Since  $\nabla \cdot \mathbf{E} = 0$  and  $\nabla \cdot \mathbf{B} = 0$  so,

$$\nabla^2 \mathbf{E} = \mu_0 \epsilon_0 \frac{\partial^2 \mathbf{E}}{\partial^2 t} \tag{2.55}$$

$$\nabla^2 \mathbf{B} = \mu_0 \epsilon_0 \frac{\partial^2 \mathbf{B}}{\partial^2 t} \tag{2.56}$$

which is similar to wave equation  $\nabla^2 f = \frac{1}{v^2} \frac{\partial^2 f}{\partial t^2}$  with  $v = \frac{1}{\sqrt{\mu_0 \epsilon_0}} = C = 3 \times 10^8 \text{m/s}$ 

#### **Energy in Electromagnetic Waves**

The Work which is required to assemble a static charge distribution configuration (against the coulomb repulsion of charges) is

 $W_e = \frac{\epsilon_0}{2} \int E^2 d\tau$  where **E** is resulting electric field

similarly, the work required to get the current going is given by

 $W_m = \frac{1}{2\mu_0} \int B^2 d\tau$  where **B** is resulting Magnetic field

In an electromagnetic field, per unit volume, the energy is given by

$$u = \frac{1}{2} \left( \epsilon_0 E^2 + \frac{1}{\mu_0} B^2 \right)$$

### 2.2.2 Poynting Vectors and Poynting Theorem

A key idea in electromagnetic theory that pertains to the transmission of energy in electromagnetic fields is the Poynting's theorem. It says that the Poynting vector, defined as the cross product of the electric and magnetic fields at any particular point, is equivalent to the

amount of energy per unit time passing through a unit area of a surface. This theory offers an important resource for comprehending electromagnetic wave behaviour and interactions with matter .S is the energy current density or flow of energy per unit time per unit area. Poynting's theorem states that The work done on the charges by the electromagnetic. force is equal to the decrease in energy stored in the field, less the energy that flowed out through the surface.

Think about a setup with some configuration charge and current. It produces electric **E** and magnetic **B** fields, which in turn act on charged particles. By doing work on the particles Electromagnetic forces lose energy. Particles on the other hand will increase their mechanical energy (kinetic and potential energy). Energy may also lose if it flows out of the volume.

On a single charge q the work done by electromagnetic forces (work done by the magnetic field is 0)

$$dW = q(\mathbf{E} + \mathbf{v} \times \mathbf{B}).d\mathbf{l} = q\mathbf{E}.d\mathbf{l} = q\mathbf{E}.\mathbf{v}dt$$

therefore,

$$\frac{dW}{dt} = q\mathbf{E}.\mathbf{v}$$

Work done on all the charges per unit time ("Power delivered"): $(J = \rho \mathbf{v})$ 

$$\frac{dW}{dt} = \int_{\mathbf{v}} \rho \mathbf{E} . \mathbf{v} d\tau = \int_{\mathbf{v}} \mathbf{E} . \mathbf{J} d\tau$$

By Maxwell's equation  $\nabla \times \mathbf{B} = \mu_0 \left( \mathbf{J} + \epsilon_0 \frac{\partial \mathbf{E}}{\partial t} \right)$  So  $\mathbf{J} = \frac{1}{\mu_0} (\nabla \times \mathbf{B}) - \epsilon_0 \frac{\partial \mathbf{E}}{\partial t}$ 

Now using formula  $\nabla \cdot (\mathbf{A} \times \mathbf{B}) = \mathbf{B} \cdot (\nabla \times \mathbf{A}) - \mathbf{A} \cdot (\nabla \times \mathbf{B})$  we can write

$$\nabla \cdot (\mathbf{E} \times \mathbf{B}) = \mathbf{B} \cdot (\nabla \times \mathbf{E}) - \mathbf{E} \cdot (\nabla \times \mathbf{B}) = -\mathbf{B} \cdot \frac{\partial \mathbf{B}}{\partial t} - \mathbf{E} \cdot (\nabla \times \mathbf{B})$$

$$\mathbf{E}.(\nabla \times \mathbf{B}) = -\nabla.(\mathbf{E} \times \mathbf{B}) - \mathbf{B}.\frac{\partial \mathbf{B}}{\partial t}$$

We can now write the

$$\mathbf{E}.\mathbf{J} = \frac{1}{\mu_0} \mathbf{E}.(\nabla \times \mathbf{B}) - \epsilon_0 \mathbf{E}.\frac{\partial \mathbf{E}}{\partial t}$$
(2.57)

$$\mathbf{E}.\mathbf{J} = \frac{1}{\mu_0} (-\nabla \cdot (\mathbf{E} \times \mathbf{B}) - \mathbf{B} \cdot \frac{\partial \mathbf{B}}{\partial t}) - \epsilon_0 \mathbf{E} \cdot \frac{\partial \mathbf{E}}{\partial t}$$
(2.58)

$$\mathbf{E}.\mathbf{J} = -\frac{1}{\mu_0} \nabla \cdot (\mathbf{E} \times \mathbf{B}) - \frac{1}{2\mu_0} \frac{\partial B^2}{\partial t} - \frac{\epsilon_0}{2} \frac{\partial E^2}{\partial t}$$
 (2.59)

Work done on all the charges per unit time ("Power delivered") is

$$\frac{dW}{dt} = \int_{V} \mathbf{E} . \mathbf{J} d\tau \tag{2.60}$$

$$\frac{dW}{dt} = \int_{V} -\frac{1}{\mu_0} \nabla \cdot (\mathbf{E} \times \mathbf{B}) - \frac{1}{2\mu_0} \frac{\partial B^2}{\partial t} - \frac{\epsilon_0}{2} \frac{\partial E^2}{\partial t} d\tau$$
 (2.61)

$$\frac{dW}{dt} = \frac{\partial}{\partial t} \int_{V} \frac{1}{2} \left( \epsilon_0 E^2 + \frac{1}{\mu_0} B^2 \right) d\tau - \oint_{S} \frac{1}{\mu_0} (\mathbf{E} \times \mathbf{B}) . d\mathbf{a}$$
 (2.62)

part in red colour is the density of energy stored in the electromagnetic fields  $(u_{em})$ , and part in blue is the Poynting vector  $\mathbf{S}$  we can write  $\frac{dW}{dt}$  as  $\frac{d}{dt} \int_{\mathbf{v}} u_{mech} d\tau$  where  $u_{mech}$  is the density of mechanical energy and  $W = U_{mech}$  is the total mechanical energy of all the particles in volume V

$$\frac{\partial}{\partial t} \int_{\mathbf{v}} (u_{mech} + u_{em}) d\tau = -\oint_{\mathbf{s}} \mathbf{S} . d\mathbf{a} = -\int_{\mathbf{v}} (\nabla . \mathbf{S}) d\tau$$
 (2.63)

$$\frac{\partial}{\partial t}(u_{mech} + u_{em}) = -\nabla.\mathbf{S} \tag{2.64}$$

Thus, Poynting's theorem is simply a conservation of energy conservation. By their own, the particles' energy and momentum have not been preserved. Rather, the particles transfer energy and momentum to the fields and the fields transfer it back to the particles. However, the combined amount of energy and momentum of the fields and the particles together is conserved.

#### 2.2.3 Lorentz Force per unit volume

The Lorentz Force on a charge q is given by  $\mathbf{F} = q(\mathbf{E} + \mathbf{v} \times \mathbf{B})$  The Force on all charge is given by  $:(\mathbf{J} = \rho \mathbf{v})$ 

$$\mathbf{F} = \int_{\mathbf{v}} \rho(\mathbf{E} + \mathbf{v} \times \mathbf{B}) d\tau = \int_{\mathbf{v}} (\rho \mathbf{E} + \mathbf{J} \times \mathbf{B}) d\tau$$

Force per unit volume is  $f = (\rho \mathbf{E} + \mathbf{J} \times \mathbf{B})$  from Maxwell's equations 2.45 and 2.48, we can write  $\rho = \epsilon_0(\nabla \cdot \mathbf{E})$  and  $\mathbf{J} = \frac{1}{\mu_0}(\nabla \times \mathbf{B}) - \epsilon_0 \frac{\partial \mathbf{E}}{\partial t}$ 

$$f = \epsilon_0(\nabla \cdot \mathbf{E})\mathbf{E} + \left(\frac{1}{\mu_0}(\nabla \times \mathbf{B}) - \epsilon_0 \frac{\partial \mathbf{E}}{\partial t}\right) \times \mathbf{B}$$
 (2.65)

$$\frac{\partial \mathbf{E}}{\partial t} \times \mathbf{B} = \frac{\partial}{\partial t} (\mathbf{E} \times \mathbf{B}) - \frac{\partial \mathbf{B}}{\partial t} \times \mathbf{E} = \mu_0 \frac{\partial \mathbf{S}}{\partial t} + \mathbf{E} \times (\nabla \times \mathbf{E})$$
 (2.66)

$$f = \epsilon_0(\nabla \cdot \mathbf{E}) - \frac{1}{\mu_0} \mathbf{B} \times (\nabla \times \mathbf{B}) - \mu_0 \epsilon_0 \frac{\partial \mathbf{S}}{\partial t} - \epsilon_0 \mathbf{E} \times (\nabla \times \mathbf{E}) + \frac{1}{\mu_0} (\nabla \cdot \mathbf{B}) \mathbf{B}$$
 (2.67)

using the equation

$$\nabla(\mathbf{A}.\mathbf{B}) = \mathbf{A} \times (\nabla \times \mathbf{B}) + \mathbf{B} \times (\nabla \times \mathbf{A}) + (\mathbf{A}.\nabla)\mathbf{B} + (\mathbf{B}.\nabla)\mathbf{A}$$

$$\nabla E^2 = \nabla (\mathbf{E}.\mathbf{E}) = 2\mathbf{E} \times (\nabla \times \mathbf{E}) + 2(\mathbf{E}.\nabla)\mathbf{E}$$
 (2.68)

$$\mathbf{E} \times (\nabla \times \mathbf{E}) = \frac{1}{2} \nabla E^2 - (\mathbf{E} \cdot \nabla) \mathbf{E}$$
 (2.69)

similarly,

$$\mathbf{B} \times (\nabla \times \mathbf{B}) = \frac{1}{2} \nabla B^2 - (\mathbf{B} \cdot \nabla) \mathbf{B}$$
 (2.70)

we can write the equation for f as

$$f = \epsilon_0(\nabla \cdot \mathbf{E}) - \frac{\epsilon_0}{2} \nabla E^2 + \epsilon_0(\mathbf{E} \cdot \nabla) \mathbf{E} + \frac{1}{\mu_0} (\nabla \cdot \mathbf{B}) \mathbf{B} - \frac{1}{2\mu_0} \nabla B^2 + \frac{1}{\mu_0} (\mathbf{B} \cdot \nabla) \mathbf{B} - \mu_0 \epsilon_0 \frac{\partial \mathbf{S}}{\partial t}$$
(2.71)

$$f = \epsilon_0(\nabla \cdot \mathbf{E}) + \epsilon_0(\mathbf{E} \cdot \nabla)\mathbf{E} + \frac{1}{\mu_0}(\nabla \cdot \mathbf{B})\mathbf{B} + \frac{1}{\mu_0}(\mathbf{B} \cdot \nabla)\mathbf{B} - \nabla\left(\frac{\epsilon_0}{2}E^2 + \frac{1}{2\mu_0}\nabla B^2\right) - \mu_0\epsilon_0\frac{\partial \mathbf{S}}{\partial t}$$

Maxwell stress tensor, in terms of physics, is the force per unit area (stress) operating on the surface. we can define a Maxwell Stress Tensor

$$T_{ij} = \epsilon_0 \left( E_i E_j - \frac{\delta_{ij}}{2} E^2 \right) + \frac{1}{\mu_0} \left( B_i B_j - \frac{\delta_{ij}}{2} B^2 \right)$$

where  $T_{ij}$  is the  $i^{th}$  component of stress on  $j^{th}$  component of area element

$$\nabla. \stackrel{\leftrightarrow}{\mathbf{T}} = \epsilon_0(\nabla.\mathbf{E}) + \epsilon_0(\mathbf{E}.\nabla)\mathbf{E} + \frac{1}{\mu_0}(\nabla.\mathbf{B})\mathbf{B} + \frac{1}{\mu_0}(\mathbf{B}.\nabla)\mathbf{B} - \nabla\left(\frac{\epsilon_0}{2}E^2 + \frac{1}{2\mu_0}\nabla B^2\right)$$

so Force per unit volume is

$$f = \nabla \cdot \stackrel{\leftrightarrow}{\mathbf{T}} - \mu_0 \epsilon_0 \frac{\partial \mathbf{S}}{\partial t}$$
 (2.72)

The Total force on the charges in volume V is therefore given by

$$F = \int_{\mathbf{V}} \nabla \cdot \stackrel{\leftrightarrow}{\mathbf{T}} d\tau - \mu_0 \epsilon_0 \frac{d}{dt} \int_{\mathbf{V}} \mathbf{S} d\tau$$
 (2.73)

$$F = \frac{\mathbf{dP_{mech}}}{dt} = -\frac{d}{dt} \int_{\mathbf{v}} \epsilon_0 \mu_0 \mathbf{S} d\tau + \oint_{\mathbf{s}} \mathbf{T} . d\mathbf{a}$$
 (2.74)

the green part is  $\vec{p}_{em}$  density of momentum stored in electromagnetic field

$$\frac{d}{dt} \int_{V} (\vec{p}_{mech} + \vec{p}_{em}) d\tau = \oint_{s} \stackrel{\leftrightarrow}{\mathbf{T}} . d\mathbf{a}$$
 (2.75)

 $\mathbf{dP_{mech}}$  is the total (mechanical) momentum of the particles in V  $\vec{p}_{mech}$  is the (mechanical) density of momentum of particles in volume V.

 $\mathbf{S} = \frac{1}{\mu_0}(\mathbf{E} \times \mathbf{B})$  Poynting vector is the flow of electromagnetic energy per unit time unit area and also  $\vec{p}_{em} = \epsilon_0 \mu_0 \mathbf{S} = \epsilon_0(\mathbf{E} \times \mathbf{B})$  is the density of momentum stored in the electromagnetic field. The momentum of the electromagnetic field is along the same direction as that of the pointing vector.

#### 2.2.4 Monochromatic plane wave

Electromagnetic radiation with a single frequency and a single direction of propagation in a plane perpendicular to the wave's vibration direction is known as monochromatic plane electromagnetic waves. Both the magnetic and electrical fields fluctuate in phase and are perpendicular to one another in these waves, which is a special characteristic. Common uses for monochromatic plane waves include wireless communication, radar technology, and medical imaging. The speed of light is the constant velocity of these waves in a vacuum. Due

to their special qualities, monochromatic plane waves have a wide variety of applications and are a crucial topic of research in the fields of engineering and physics.

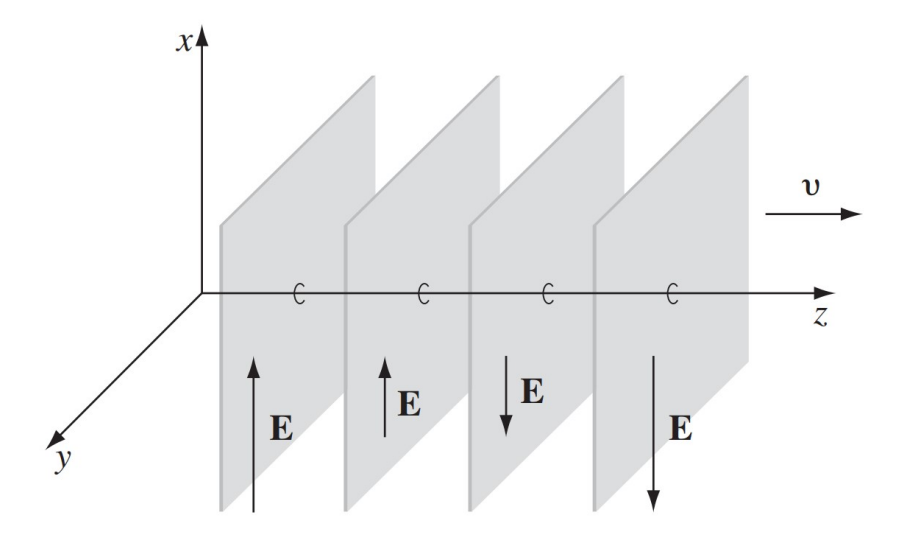


Figure 2.6: Monochromatic Plane Electromagnetic Wave[15]

If in an arbitrary direction  $\vec{k}$  Plane monochromatic wave is propagating then

$$\mathbf{E}(\mathbf{r},t) = \mathbf{E}_0 e^{i(\mathbf{k}\cdot\mathbf{r} - wt)} \hat{\mathbf{n}}$$

$$\mathbf{B}(\mathbf{r},t) = \frac{1}{c} \mathbf{E}_0 e^{i(\mathbf{k}\cdot\mathbf{r} - wt)} (\hat{\mathbf{k}} \times \hat{\mathbf{n}})$$

where  $\hat{\mathbf{k}}$ : propagation vector,  $\hat{\mathbf{n}}$ : polarization vector and  $\hat{\mathbf{n}} \cdot \hat{\mathbf{k}} = 0$ 

Plane Monochromatic waves travelling along,

$$\mathbf{E}(z,t) = \mathbf{E}_0 \cos(kz - wt + \delta)\hat{\mathbf{x}}$$

$$\mathbf{B}(z,t) = \frac{1}{c} \mathbf{E}_0 \cos(kz - wt + \delta)\hat{\mathbf{y}}$$

electromagnetic energy density is [\* is  $(kz - wt + \delta)]$ 

$$u_{em} = \frac{1}{2} \left( \epsilon_0 E^2 + \frac{1}{\mu_0} B^2 \right) = \frac{1}{2} \left( \epsilon_0 E_0^2 \cos^2(*) + \frac{1}{\mu_0 c^2} E_0^2 \cos^2(*) \right) = \epsilon_0 E_0^2 \cos^2(*)$$

S: the flow of electromagnetic energy per unit time per unit area

$$\mathbf{S} = \frac{1}{\mu_0} (\mathbf{E} \times \mathbf{B}) = \frac{1}{\mu_0 c} E_0^2 \cos^2(*) \hat{\mathbf{z}} = c u_{em} \hat{\mathbf{z}}$$

Assume a cylindrical structure that is parallel with the z-axis and has a unit cross-section area and length c. The entire amount of energy held in the cylinder is represented by the flow of e.m. energy per unit time per unit area  $(= cu_{em})$ .

electromagnetic momentum density will be  $\epsilon_0 \mu_0 \mathbf{S} = \frac{1}{c} u_{em} \hat{\mathbf{z}}$ 

By averaging over many complete cycles we know  $\langle cos^2(*) \rangle = \langle sin^2(*) \rangle = \frac{1}{2}$ 

so 
$$\langle u_{em} \rangle = \frac{1}{2} \epsilon_0 E_0^2$$
 and  $\langle \mathbf{S} \rangle = \frac{1}{2} c \epsilon_0 E_0^2 \hat{\mathbf{z}}$  and average momentum density  $\langle p_{em} \rangle = \frac{1}{2c} \epsilon_0 E_0^2 \hat{\mathbf{z}}$ 

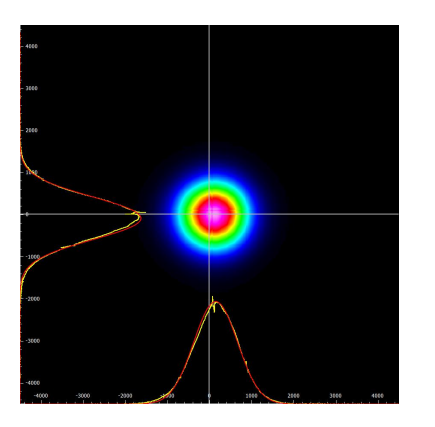
Intensity =  $\langle Power per unit area transported by an electromagnetic wave \rangle$ 

Intensity =  $\langle \text{Energy per unit time per unit area transported} \rangle I = \langle |\mathbf{S}| \rangle$ 

for a plane monochromatic wave Poynting vector which is perpendicular to the plane wavefront so the momentum density is along the direction of the Poynting vector also perpendicular to the wavefront which is along z direction so it has only linear momentum and no angular momentum.

#### 2.2.5 Gaussian Light Beam

The study of Gaussian beams, a particular kind of laser beam with a particular intensity distribution, is the focus of the optics branch known as "Gaussian beam optics." The intensity profile of these beams is bell-shaped, with the centre having the highest intensity and the periphery having progressively lower intensity. Self-focusing and maintaining beam size over extended distances are just a few of the many crucial characteristics of Gaussian beams. They are extensively utilized in many different applications, including laser surgery, material processing, and cutting with a laser. Understanding how these beams move through various optical components, such as lenses, and mirrors, as well as how their characteristics alter when they contact with diverse materials, is a necessary part of the study of Gaussian beam optics.



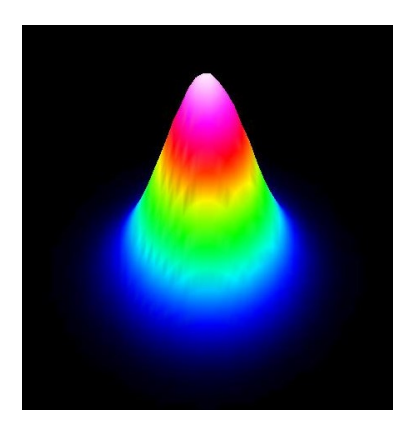


Figure 2.7: Gaussian beam intensity profile

The equation for plane wave is  $E(\vec{r}) = E_0(\vec{r})e^{-ikz}$  for such plane wave  $E_0$  is constant in xy plane But by solving the Helmholtz equation with paraxial approximation

$$(\nabla^2 + k^2)E(x, y, z) = 0$$

we will get Gaussian beam is one of the solution

The equation for the Gaussian wave is

$$E(r,z) = E_0 \frac{\omega_0}{\omega(z)} e^{i\Phi(z)} e^{-\frac{r^2}{\omega(z)^2}} e^{-i\frac{kr^2}{2R(z)}} e^{ikz}$$

We can write the Normalized Gaussian beam as

$$\frac{E(x,y,z)}{E_0} = \frac{\omega_0}{\omega(z)} e^{\left[-\frac{r^2}{\omega^2(z)}\right]} e^{\left[-i\frac{kr^2}{2R(z)}\right]} e^{i[kz-\Phi(z)]}$$
(2.76)

here,n is the refractive index and  $\lambda_0$  is the wavelength of the beam.

$$\omega(z) = \omega_0 \sqrt{1 + (\frac{z}{z_R})^2}$$
 is the spot size

 $R(z) = z[1 + (\frac{z_R}{z})^2]$  is the radius of curvature

$$\Phi(z) = tan^{-1}(z/z_R)$$
 is the Guoy phase shift

 $z_R = \frac{\pi n \omega_0^2}{\lambda_0}$  is the Rayleigh length of the Gaussian beam

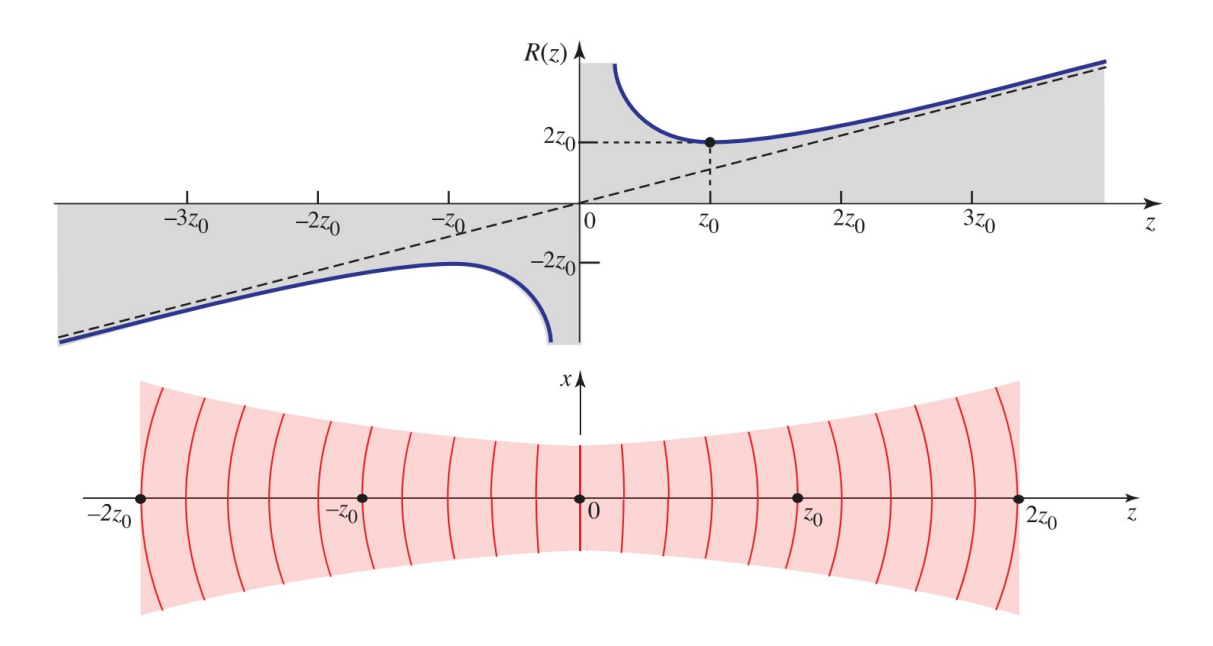


Figure 2.8: The Gaussian Beam's wavefronts and plot between the radius of curvature of wavefront and position along the beam axis. The dotted line is for the spherical wavefront where it is linear[16]

At z=0 radius of curvature R(z) is  $\infty$  so wavefronts are planer. at the Rayleigh length, the radius of curvature becomes the minimum value of twice of Rayleigh length then it increases linearly with z. For very large z we can approximate it as spherical waves. but for z much smaller than Rayleigh length we can treat it as a plane wave thereby S Poynting vector is always perpendicular to the plane wavefront, so it has only linear momentum in the wave which can be used to trap dielectric particles.

#### 2.2.6 Laguerre Gaussian Beam

Laguerre Gaussian Beam is the solution to the Helmholtz equation solved under cylindrical symmetry with paraxial approximation. A laser beam type known as a Laguerre Gaussian Beam is distinguished by its helical phase front as well as annulus intensity distribution. This beam is created by the superposition of Laguerre-Gaussian modes, which are cylindrical coordinate solutions to the paraxial wave equation. In addition to its capacity to transport orbital angular momentum (OAM) and its capacity to keep its shape across lengthy propagation distances, the Laguerre Gaussian Beam has numerous other special qualities. Due to

these characteristics, the Laguerre Gaussian Beam is perfect for a number of uses, including optical communication, quantum information processing, and optical trapping. Understanding the features of the Laguerre Gaussian Beam, how it interacts with various materials and optical components, and designing and optimizing optical systems based on it are all part of the study of this phenomenon.

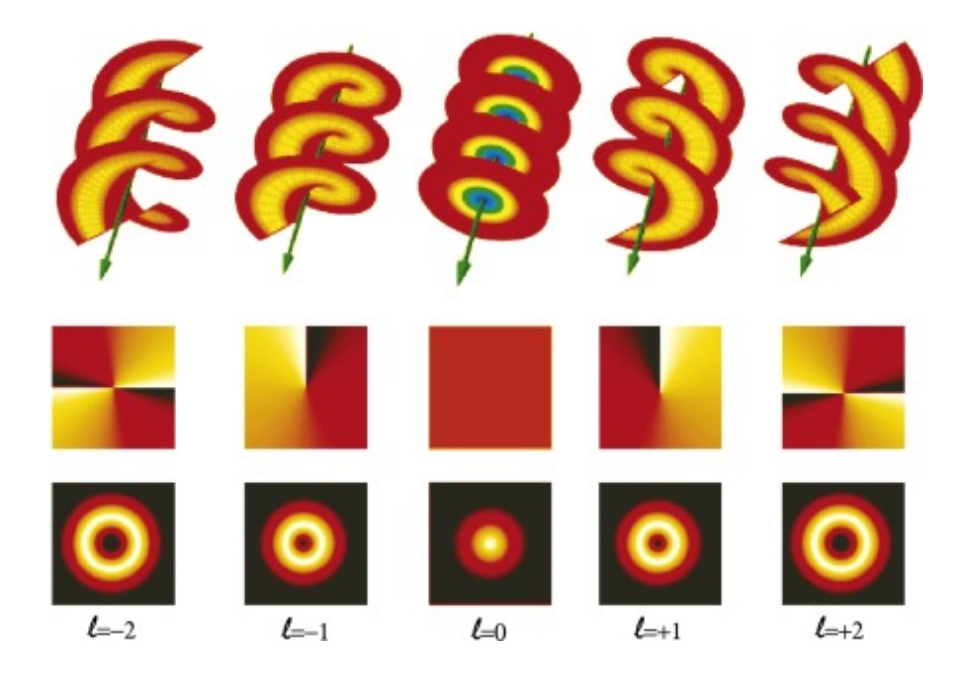


Figure 2.9: Laguerre Gaussian Beam [17]

The equation of the Laguerre Gaussian Beam can be written as

$$E(r,\phi,z) = \sqrt{\frac{2p!}{\pi(p+|l|)!}} \frac{1}{\omega(z)} e^{-\frac{r^2}{w^2(z)}} \left(\frac{r\sqrt{2}}{\omega(z)}\right)^{|l|} L_{p,|l|} \left[\frac{2r^2}{\omega^2(z)}\right] e^{il\phi}$$
(2.77)

The brown part is the normalization, the blue part is Gaussian, the green part is the doughnut hole for |l| > 0 cyan color part is the Laguerre polynomial (= 1 for p = 0), the red part is the spiral phase which results in helical structured in the beam. I and p are the azimuthal and radial mode index respectively.

In 1905, John Poynting developed the theory of electromagnetic radiation pressure and momentum density, which Albert Einstein later supported, explaining the linear momentum of a photon is  $\hbar k$ . Light's linear momentum has been used to trap and cool atoms and

molecules. Poynting also realized that polarized light has spin angular momentum, while in 1992, a group at Leiden University recognized that light beams with helical phase fronts have an orbital angular momentum of  $L=l\hbar$  per photon independent of polarization. The beams have intertwined helical phase fronts, leading to an annular cross-sectional intensity pattern that persists regardless of how tightly the beam is focused. This on-axis singularity is a specific instance of phase dislocation, leading to a simple annular intensity profile, but when made to interfere with a plane wave, it produces a spiral intensity pattern. Light beams with quantized orbital angular momentum have been produced, providing a means to investigate new optical interactions. The Poynting vector produces an orbital angular momentum parallel to the beam axis, creating an optical vortex. The Laguerre-Gaussian (LG) laser mode is the most common form of a helically phased beam. the spin angular momentum associated with the circular polarization of light has the momentum of  $\pm \hbar$  based on polarization.

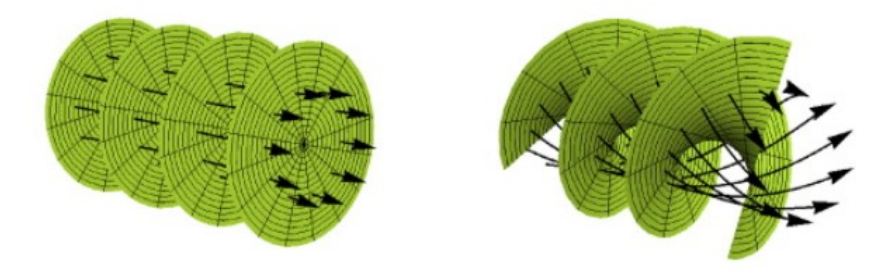


Figure 2.10: Pointing vector in Laguerre Gaussian Beam spirals due to the helicity of wavefront[18]

The momentum density of light is along the direction of Poynting vector. The Poynting vector (arrows) is no longer parallel to the beam axis (in-plane waves it is parallel to the beam axis). At any fixed radius within the beam, the Poynting vector follows a spiral trajectory around the axis in Laguerre Gaussian Beam so it also has orbital angular momentum

## 2.3 Optical Tweezer

In this Section, we will outline the principle of holographic optical tweezer and time-shared optical traps created by AOD. Arthur Ashkin invented the optical Tweezers technique in 1986 for the manipulation of micro-particles, and then eventually used it to manipulate atoms, molecules, and biological cells. The Principle of this technique is the radiation pressure of light[19, 20, 21].

#### 2.4 Radiation Pressure

The Pressure applied by an electromagnetic wave on the object due to the transfer of momentum between matter and the electromagnetic field

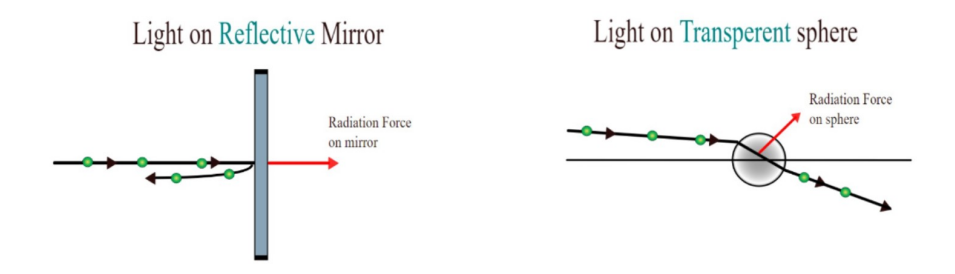


Figure 2.11: a)radiation pressure on material which reflective Light b)radiation pressure on transparent sphere

When a Photon incident on the reflecting surface normally it reflects back so its momentum is reversed and the reflecting surface experiences recoiling due to the conservation of momentum.

When a photon incident on the transparent sphere as in the figure 2.13(b) due to refraction it bends towards the center of the sphere so it changes its direction thereby its momentum also changes. If the photon enters the sphere upside of a sphere it leaves the sphere downwards so by momentum conservation the sphere moves upwards and forward if the photon enters the sphere downside of a sphere it leaves the sphere upwards so the sphere moves downwards and forward.

If two photons simultaneously and symmetrically enter both upward and downward of the sphere then the sphere moves forward as the upward and downward components cancel each other[20].

## 2.5 Optical trapping in Geometric optics region

Here the size of the trapping particle is greater than the wavelength of the electromagnetic wave used to trap the particle.<sup>1</sup>

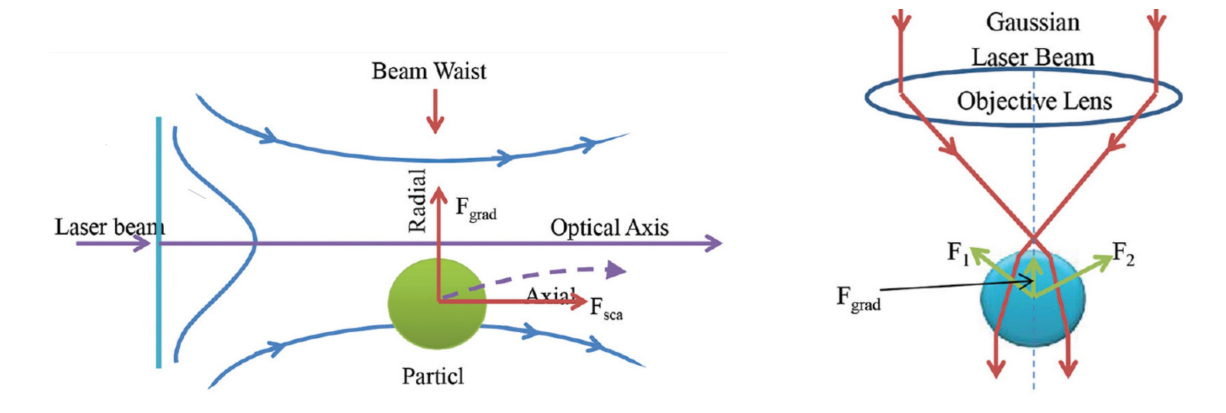


Figure 2.12: a)scattering and Gradient force on a transparent sphere b)gradient force due to focusing balances the scattering force

The laser beam is not plane waves and its intensity is not uniform in the transverse direction. Lasers have a spatial mode of cavity usually  $TM_{00}$  Gaussian mode distribution. So the transparent sphere is located not at the centre of the Gaussian beam as in the figure 2.12(a) more photons are in up compared to in the bottom of the sphere. So the Net effect of gradient force is towards the centre of the Gaussian beam and due to scattering force the sphere moves forward.

If we tightly focus the beam using the High NA objective then there is some point after the focus where the scattering force is nullified by the gradient force which was created due to tight focusing along the direction of the scattering force leading to optical tweezers trap[22].

<sup>&</sup>lt;sup>1</sup>https://www.ijhonline.org/viewimage.asp?img=IraqiJHematol\_2018\_7\_2\_79\_239528\_f1.jpg

## 2.6 Optical trapping in Rayleigh regime

In this case, the size of the particle is smaller than or comparable to the wavelength of the electromagnetic wave used to trap the particle. The ray optical technique is less effective for particles smaller than the laser beam's wavelength, and it is preferable to think of the forces in terms of the electric field and electric dipoles that surround the trapped particle. A dipole moment is created in the particle by the electromagnetic radiation's electric field. (to be trapped). This dipole is drawn to the area of a light beam with the greatest intensity. The dipole will experience non-zero force  $(F = \mu.\nabla E)$  because the E field of the electromagnetic wave is not homogeneous for the light utilised for trapping.

**Gradient force:** Let the polarizability of the trapping particle is  $\alpha$  and the electric field of electromagnetic field will be **E** then the Induced dipole moment  $(\vec{\mu})$  is  $\vec{\mu} = \alpha \mathbf{E}$ . The Potential energy of the particle due to electric field **E** is

$$V = -\frac{1}{2}\vec{\mu}.\mathbf{E} = \frac{1}{2\epsilon_0 c} - re(\alpha)I$$

The force experienced is  $F = -\nabla V$  so  $F_{grad} \approx \frac{\alpha}{2} \nabla I$  Here I is the field intensity  $I = \frac{1}{2} \epsilon_0 c |\mathbf{E}|^2$ , c is speed of electromagnetic waves,  $\epsilon_0$  is permittivity of vacuum, E is field amplitude

Scattering force: the net momentum on a particle if N number of photon incident on the particle is  $P = \frac{Nh}{\lambda}$  so the scattering force is  $F_{scatter} = \frac{-dP}{dt}$  -ve sign indicates photon loses energy. The power of the beam is  $W = \frac{d(Nh\gamma)}{dt}$  so the scattering force if all photon will absorb is  $F_{scatter} = \frac{-Wn}{c}$  here n is refractive index

Time Shared Optical trap: For time-shared optical trap, the single Gaussian optical trap is shared very fast between many traps compared to the relaxation of the trapped particle so that the trapped particle will feel the time-averaged potential trap.

## 2.7 Holographic Optical Tweezers

With the use of a spatial light modulator, Holographic Optical Tweezers (HOT) [23, 14, 24, 25] are capable of controlling many small particles using a pattern of laser beams. The pattern of interference generates stable trap sites that may be precisely manipulated and

assembled in any way. In biology, materials science, and optics, HOT is used. Multiple trapping, high accuracy, adaptable patterns, and non-invasiveness are benefits of HOT over conventional optical tweezers. The plane of the Spatial light modulator has an inverse Fourier transform of the trapping plane.

#### 2.7.1 Gerchberg-Saxton (GS)Algorithm

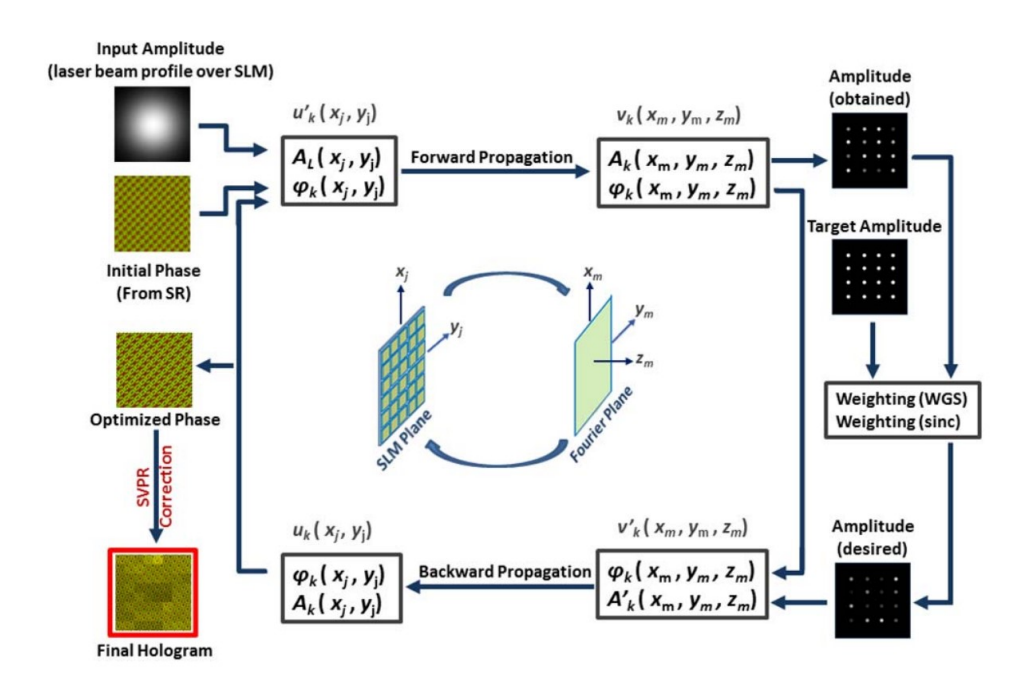


Figure 2.13: Weighted Gerchberg-Saxton (GS)Algorithm[25]

Ralph Gerchberg and Owen Saxton created the Gerchberg-Saxton algorithm, a technique for calculating the phase distribution of an electron beam or light provided the intensity distributions in two planes. It may be used to make holograms for trapping and expanded to 3D trap geometries. The procedure requires switching back and forth between two planes while propagating the complex amplitude, replacing the intensity in the trapping plane with the target intensity and that in the SLM plane with the actual intensity profile of the illuminating laser beam. The computer's graphic processing unit may be used to speed up the procedure, which converges after a few tens of iterations. By restricting the amplitude of the field on either the SLM or trapping plane, a phase-modulating hologram may produce

a variety of focus areas on the sample plane. The incoming laser beam's amplitude profile determines the amplitude on the SLM plane, whereas the target amplitudes sought for the trapping pattern define the amplitude on the trapping plane.

- To begin, a field termed  $u'_k(x_j, y_j)$  is formed as the incident laser beam on the Spatial light modulator, with an amplitude profile  $A_L(x_j, y_j)$  and a phase selected  $\Phi_k(x_j, y_j)$  at from the random superposition algorithm.
- Then, this field is transformed from the Holographic plane to the focusing plane to create a new field named  $v_k(x_j, y_j, z_j) = A_k(x_j, y_j, z_j) e^{i\Phi_k(x_j, y_j, z_j)}$ .
- A weight mixed form of the acquired amplitude and the intended amplitude is employed at the trapping plane to replace the amplitude while accounting for diffraction issues brought on by the SLM's pixelation and obtained phase is kept the same as obtained  $v'_k(x_j, y_j, z_j) = A'_k(x_j, y_j, z_j)e^{i\Phi_k(x_j, y_j, z_j)}$ .
- The computed field  $v_k'$  is transmitted back to the holographic plane to create the new field  $u_k(x_j, y_j) = A_k(x_j, y_j) e^{i\Phi_k(x_j, y_j)}$ .
- To get the final field  $u_0$  for this iteration, the laser beam amplitude profile  $A_L(x_j, y_j)$  is substituted for the amplitude profile  $A_k(x_j, y_j)$  at the SLM (holographic plane) plane.
- these steps a repeated till it converges in most cases it converges in a few iterations.

To do this Fourier transform relation between the SLM plane and trapping plane we use the Fourier lens as we discussed in the Fourier optics section.

# Chapter 3

# **Experimental Details**

#### 3.1 Colloids and Brownian motion

Colloidal suspensions, commonly referred to as colloids, are a special kind of combination in which particles are equally distributed throughout a medium, usually a liquid. Colloids differ from solutions and suspensions in that their particles are bigger than those in solutions but smaller than those in the latter. Colloids have fascinating characteristics, including the capacity to scatter light and maintain stability for extended times without settling. Colloids are a good model system that can mimic atomic systems in many properties and they are much bigger and slower than atoms so under an optical microscope itself we can see them. There are many examples of colloids in daily life, such as milk, mayonnaise, fog, and paint. Colloid science, the study of colloids, is important in a variety of fields, including the food and beverage industry, medicines, cosmetics, and environmental research. Colloids are an interesting and crucial subject of research since it is crucial to comprehend their behaviour and characteristics in many scientific and industrial domains.

A physical phenomenon known as Brownian motion, commonly referred to as Brownian diffusion, is the random movement of microscopic particles floating in a fluid medium, which is fueled by the thermal energy of the nearby molecules. Robert Brown, a Scottish botanist, first identified it in 1827 while studying pollen grains moving erratically in water under a microscope. Due to the fast-moving fluid molecules' continual bombardment of the suspended particles, which results in their unpredictable, zigzag paths, Brownian motion is created.

Temperature, particle size, and medium viscosity are only a few of the variables that affect how the particles move. Diffusion is a phenomenon that develops as a result of the dispersion and mixing of particles in a fluid caused by Brownian motion over time. Brownian motion is essential to our comprehension of many natural and artificial processes, including colloidal stability, drug administration, and nanoparticle production. It has important implications for domains including physics, chemistry, and biology.

# 3.2 Making of sample wells using Photolithography and making dense colloidal amorphous solid

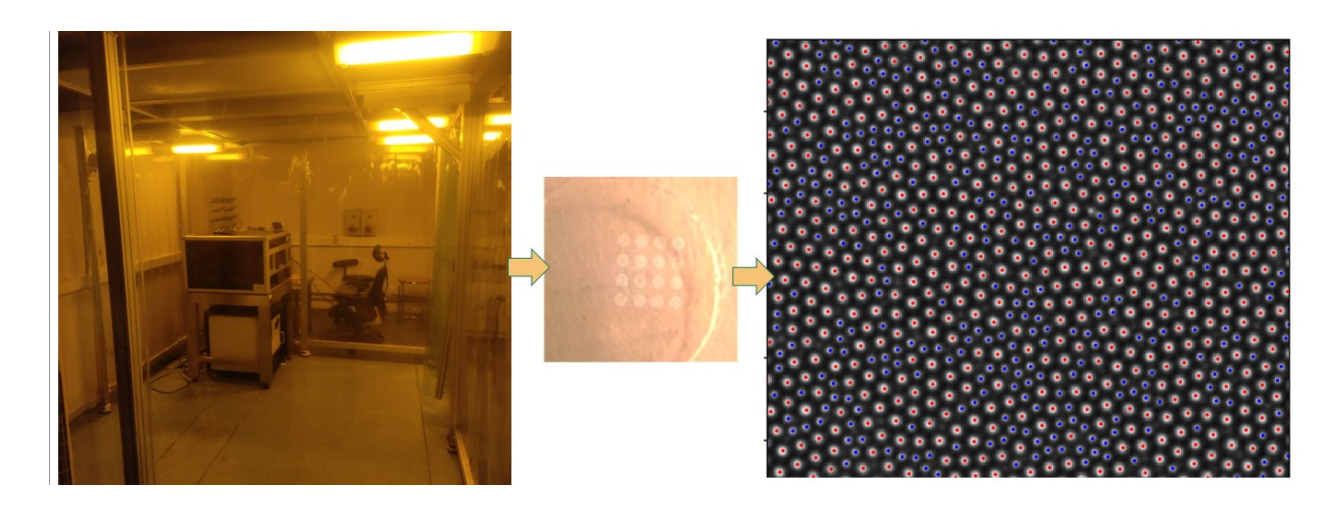


Figure 3.1: sample wells made by Photo-Lithography and silica colloidal of diameter  $3.34\mu m (\text{Red})$  and  $2.32\mu m (\text{Blue})$  to form a colloidal amorphous solid

We want to make a dense homogeneous area fraction of colloids so to make the sample wells we are using photo-lithography. We use MICROPOSIT S1813 photoresist which is a positive photoresist to spin coat the clean (by acetone and IPA) glass substrate of  $25 \times 25$  mm dimension (Corning  $25 \times 25$  mm Thickness 2 Cover Glass) at 1000rpm for 20 seconds. Then in a clean yellow room, LaserWriter 405 nm wavelength laser was to write the pattern of the circle of radius  $1000 \mu m$  surrounded by concentric rings of pattern to avoid particles further entering while taking the measurement. Then we develop the pattern using MICROPOSIT MF-319 DEVELOPER for one minute and clean the sample with deionized (DI) water to get  $2\mu m$  height wells and to avoid sticking we do oxygen plasma cleaning. Now we add

bi-dispersed  $SiO_2$  colloids (microparticles) of diameter 2.32 and 3.34  $\mu m$  in a 65:35 ratio (to kill crystallization) in deionized water and wait for 3-5 minutes to make all colloidal enter and make a dense amorphous solid (glass) well before taking measurements

## 3.3 Holographic Optical Tweezer

For the Holographic Optical tweezer, we use a 1064nm infrared laser (MATRIX-1064 Diode-Pumped Solid State Q-switched LASER 10W continuous wave mode) and use Spatial light Modulator(SLM) (The Holoeye PLUTO phase-only LCOS (Liquid Crystal on Silicon) with (1920 x 1080 pixel) and 8 µm pixel pitch). To increase the resolution of the holographic optical trap we increase the beam size using telescopic beam expansion (2.5cm and 5cm lens) configuration (2x) we need to trade-off between the resolution and efficiency of the laser in the first order if we expand largely then it either goes to zeroth order or it does not go through the active area of SLM. We are using a half-wave plate before SLM, As incident light on SLM needs to plane polarised and align with the liquid crystals in SLM to have a maximum efficiency of SLM. The plane of SLM has an inverse Fourier transform of the trapping plane. then using spatial filters we remove the zeroth and other order and take only the first order as in figure 3.4. We reduce the size and collimate using 4F configuration so that the LG beam just falls on a complete back aperture of high NA objective (Olympus 60x 0.70NA) and we collect the image of the sample using a bright field microscope (OLYMPUS IX71 inverted microscope) with CMOS camera (BASLER acA2040) and take data at 10 frames per second. We made an optical shutter to stop the laser after taking a certain amount of frames through the camera by sending on signal (digital on +5V) from LabVIEW Dagcard to Arduino and Arduino will rotate the shutter to block laser

Generation of LG Beam, from SLM: the SLM is made of liquid crystal, and based on the voltage given to each pixel of SLM the orientation varies, as a result, the phase added to light by each pixel can be controlled from 0 to  $2\pi$  as seen in figure 3.2. To create the LG beam we used the OTS-the optical tweezers software toolbox[26] to generate the pattern required to display on SLM. when no pattern is displayed then SLM acts as a mirror, when a phase of 0 to  $2\pi$  is displayed then an LG beam is created but it has both an LG beam and an unconverted Gaussian beam, so to separate the LG beam a linear grating pattern is overlapped. By this the first order contains only LG Beam as in figure 3.3 and the zero-order

is removed by spatial filters.

1

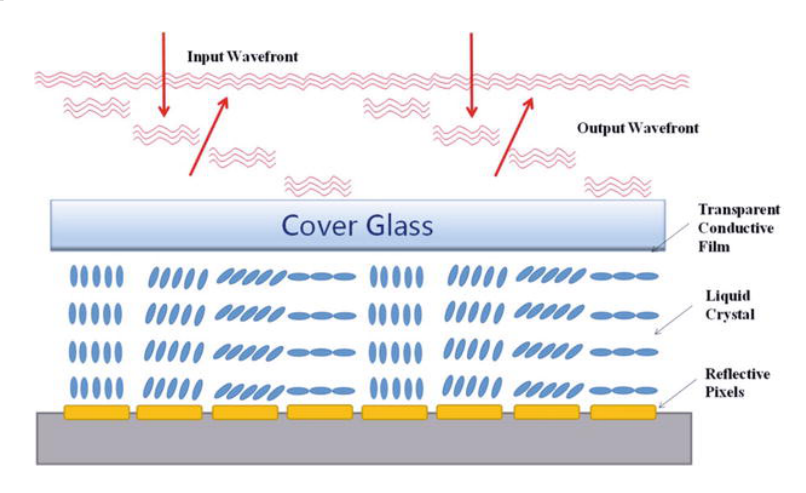


Figure 3.2: SLM based on liquid Crystal orientation add phase to light [27]

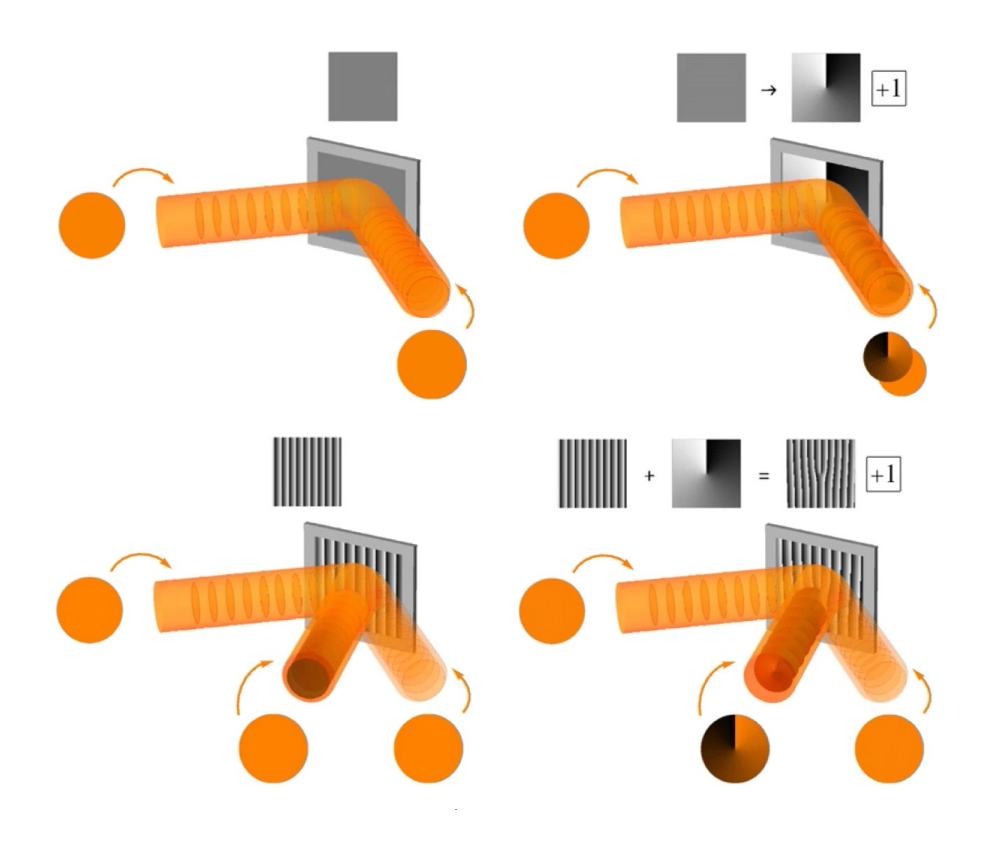


Figure 3.3: Generation Of LG beam From SLM  $\,$ 

 $<sup>\</sup>hline ^{1} https://upload.wikimedia.org/wikipedia/commons/f/fa/Generation\_of\_OAM\_beams\_using\_SLM.gif$ 

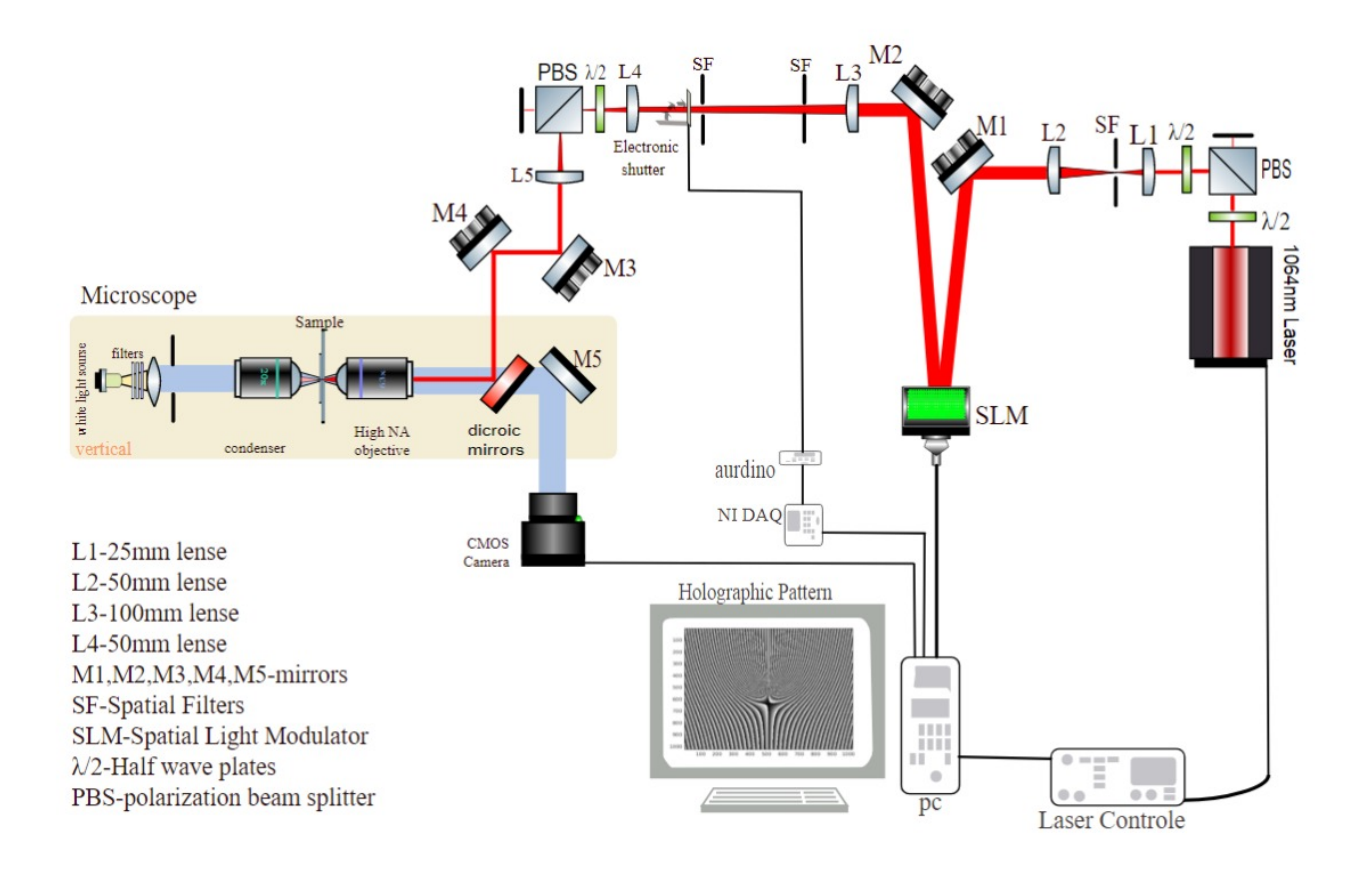


Figure 3.4: Schematics of Holographic Optical tweezer to shear the amorphous solids using LG Beam obtained by SLM.

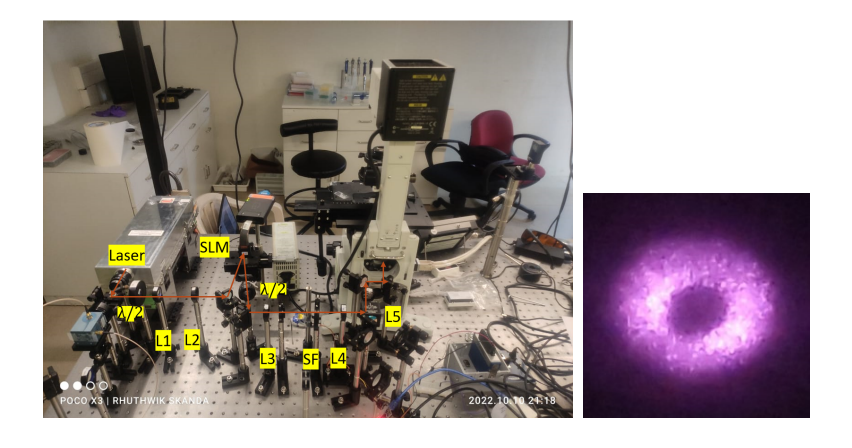


Figure 3.5: Experimental Setup for Holographic Optical tweezer to shear the amorphous solids using LG Beam obtained by SLM.

## 3.4 Time Shared Optical Traps

In this section, we discuss the instrumentation part of the Time Shared Optical Traps[28]. This setup is used to understand the crossover from crystalline to amorphous behaviours if we increase the number of particles in optical traps which will increase spring stiffness. so to create multiple optical traps with a large field of trapping and also a stiff trap of single particle trap only is discussed in this section. optical tweezers from Gaussian beam is a harmonic trap of stiffness  $k_{trap}$ , once particles get trapped they experienced a spring constant of  $k_{trap} + k$  where k is inherent stiffness due to interpartical interaction.

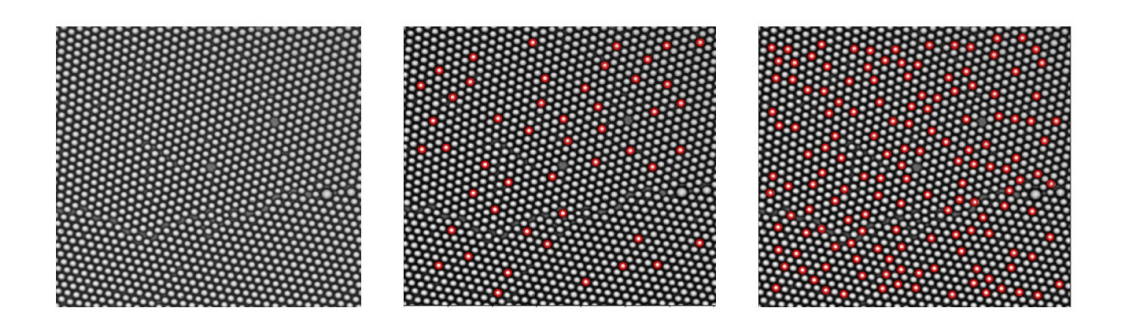


Figure 3.6: Increasing the number of random pinning of colloidal in crystals by AOD red particles are get trapped

#### Principle of working of AOD

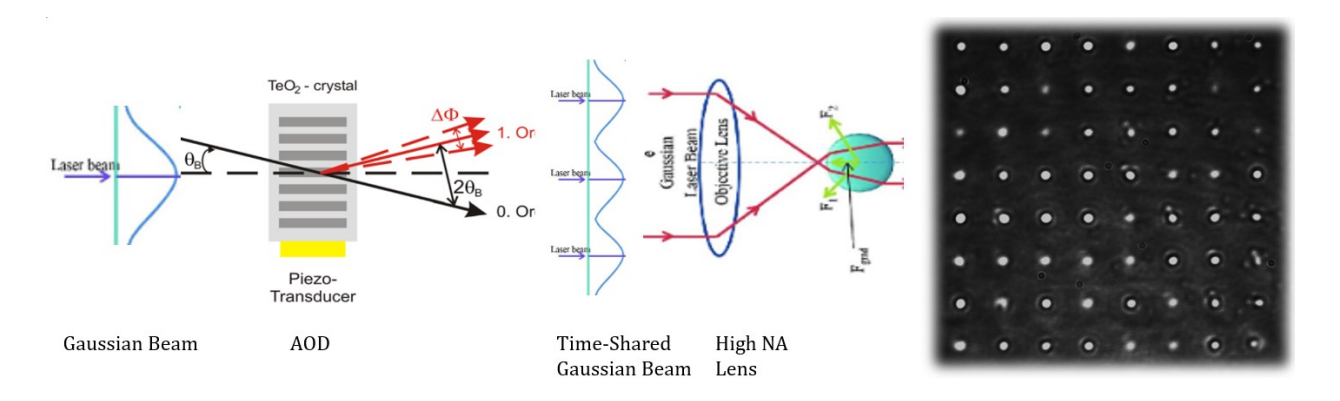


Figure 3.7: : Functionality of an AOD: The laser beam is deflected by sound waves in the TeO2– crystal inside the AOD

AOD is made of Tellurium Dioxide crystal. When RF frequency is given to a crystal, a periodic change in refractive index occurs due to compression and rarefaction of sound waves. this act as grating and is able to deflect based on the frequency of RF.

The incident laser enters the sound field at Bragg angle

$$sin\theta_B = \lambda/2\Lambda$$

Beam Separation between zero and the first order is twice the Bragg angle

$$\theta = 2\theta_B = \lambda F/V$$

where  $\lambda$ =wavelength of incident Laser, $\Lambda$ =wavelength of RF,F=frequency of RF, V=acoustic velocity of interaction medium.

For time shared Optical trap, we use Interaction DTD-274HD6M 2axis AOD which can deflect the light based on the RF frequency given to AOD. We frequency modulate the Moglabs Quad RF synthesizer using an arbitrary function generator (AFG1022 - Tektronix) to create an arbitrary pattern of the optical trap. If AFG sed +1V to RF synthesizer then +8MHz from central 27MHz will shift and -8MHz if -1V is sent.RF power used to drive is 1W per axis. The frequency of time sheared is 1000Hz.

We use 2 axis AOD (acoustic optic deflector) to deflect the 1064nm infrared laser (MATRIX-1064 Diode-Pumped Solid State Q-switched LASER 10W continuous wave mode we used 2W power) to different angles very fast and block the zeroth order undeflected light using a spatial filter and send the deflected light into the high NA objective (10x 0.85NA Leica) in a home build caged upright microscope to create optical traps. The optical traps are harmonic potential so here it is time-averaged so, particularly in trap experience time-averaged potential.RF to AOD is given using an RF synthesizer and it is Modulated using an arbitrary function generator and a function to arbitrary function generator is given using LabVIEW. Imaging is done using a Baasler acA2040 CMOS camera. The communication between AFG and RF synthesizer is done throw an SMA cable. Make confirm that the impedance is matched between these two devices. The deflected beam is sent to the High NA lens through the combination of lenses to make trap distance match the particle plane and has a high field of trapping and single particle trap (stiff trapping).

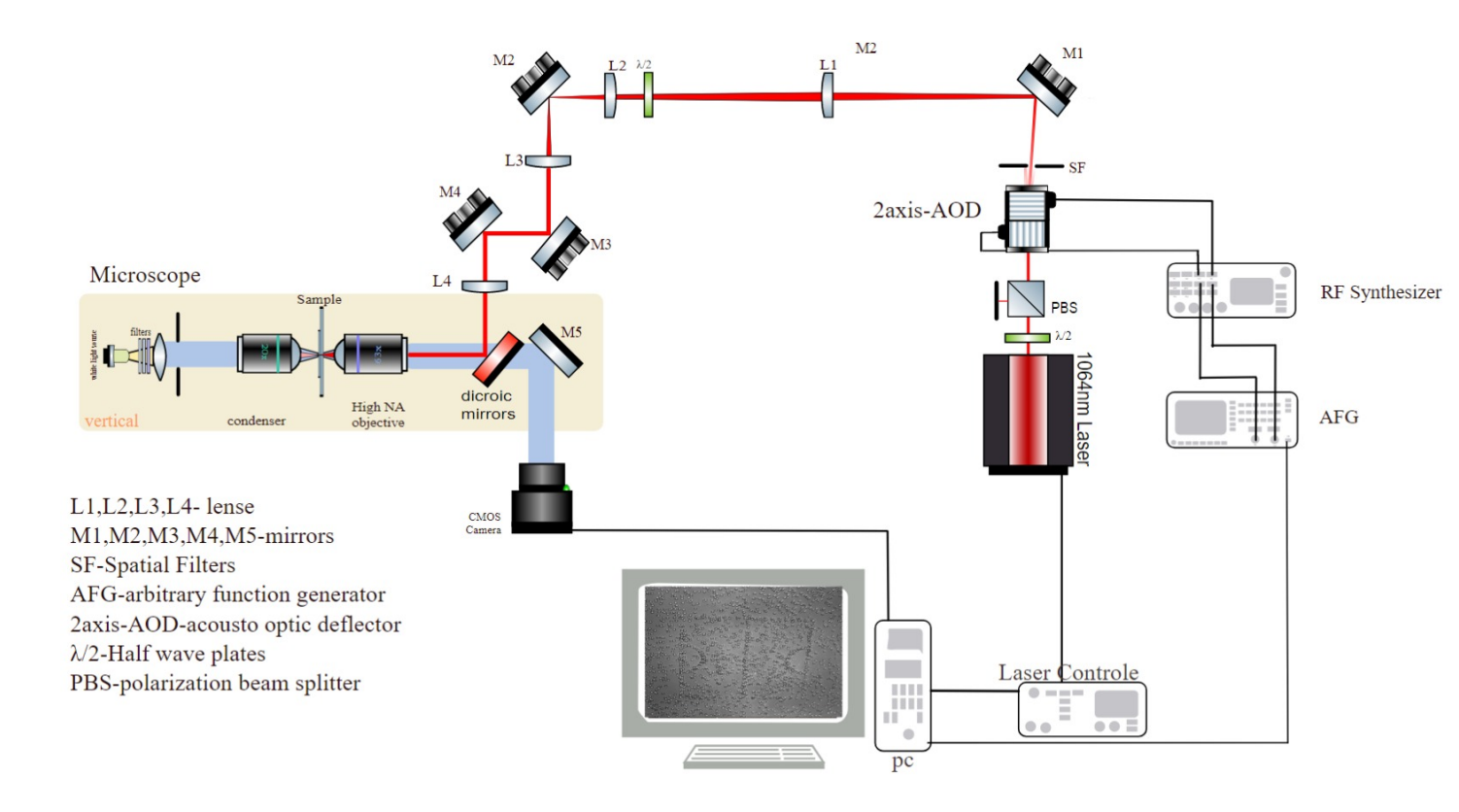


Figure 3.8: Schematics of time shared optical traps setup using 2axis AOD



Figure 3.9: Experimental Setup for time shared optical traps setup using 2axis AOD

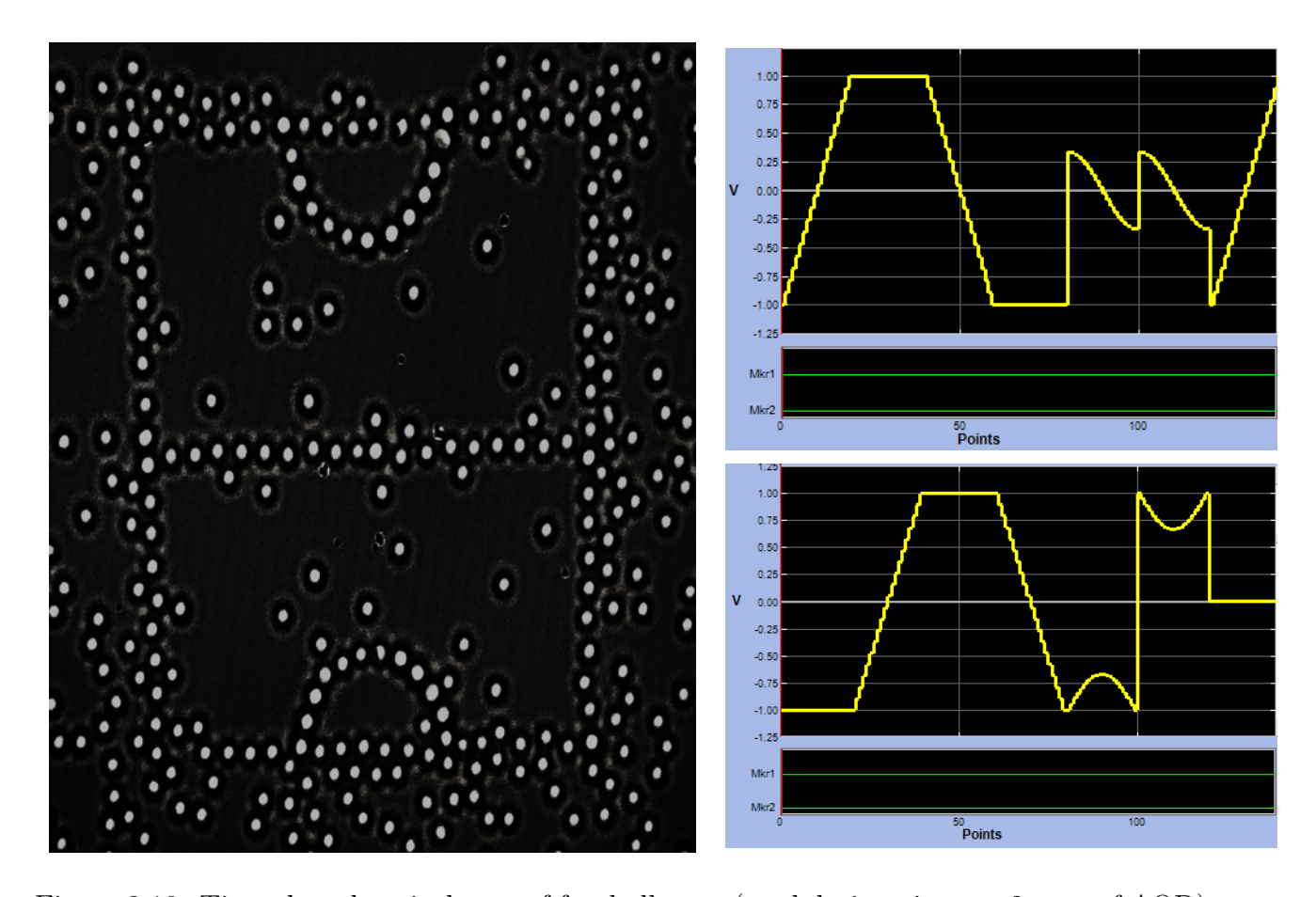


Figure 3.10: Time shared optical trap of football court(modulation given to 2 axes of AOD)

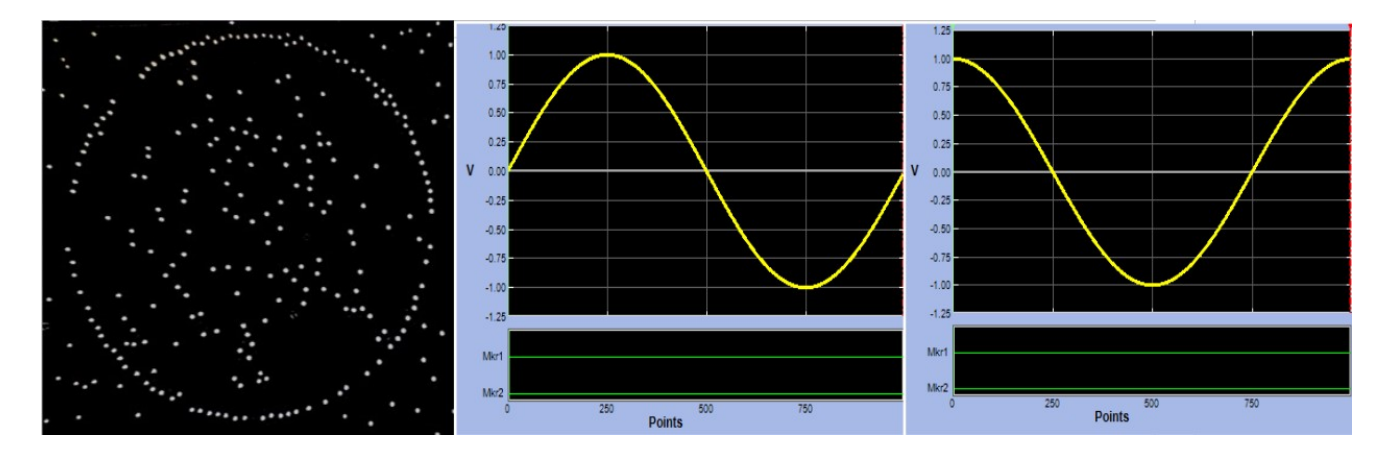


Figure 3.11: Time shared optical trap of circular shape formed by  $\sin$  and  $\cos$  modulation given to 2 axes of AOD

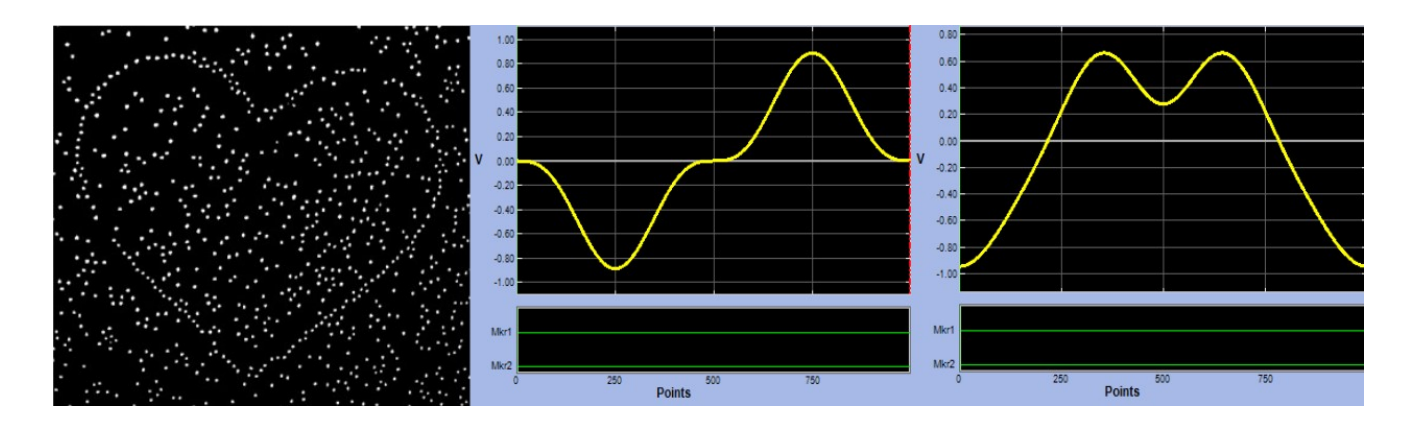


Figure 3.12: Time shared optical trap of heart shape formed by modulation given to 2 axes of AOD

To make these functions as shown in figure 3.12,3.11,3.10 I am using parametric equations. For example, for the circle, I used x = sin(t) and y = cos(t) Similarly, for other patterns we need to define an array of points in x and y and upload those arrays by LabVIEW or Arbexpress software to function generator make sure the functions used are normalized between 1 to -1. the using arbitrary mode of the arbitrary function generator changes the frequency of RF given to AOD. In RF synthesiser give the gain of frequency modulation as half the bandwidth of AOD (in this case 8MHz) so by this way when +1V is given then the frequency of RF shift by +8MHz with respect to central frequency (27MHz) and similarly in the opposite direction if -1V was given. the trap depth the particle experience is the time-averaged potential. so give the frequency of the repetition cycle to the original point as around 1K Hz. It depends on the relaxation time of the particle (i.e how fast the particle will go out of the trap if the laser is not there in that position). we are able to achieve a trapping field of view of around 150 $\mu$ m and around 200 particles were trapped in the optical traps was demonstrated in this setup.

#### 3.4.1 Data Analysis

#### g(r) Pair Correlation Function:

The description of the interior structure is typically quantified using mathematical methods such as the pair correlation function or radial distribution function. These methods allow for the calculation of the probability of encountering a different particle at a distance r from the centre of a specific particle. In the case of hard spheres, the minimum distance between two points may be equal to the diameter of the spheres. As we move farther away from a given particle, the layers become less dense, resulting in a constant probability of finding two spheres at a particular distance. The pair correlation function provides a quantification of the surroundings of the particle of interest, with a constant value across all radial lengths. At long distances or under conditions of uniform density, the pair correlation function approaches a value of 1, which is normalized by the  $\rho$  density.

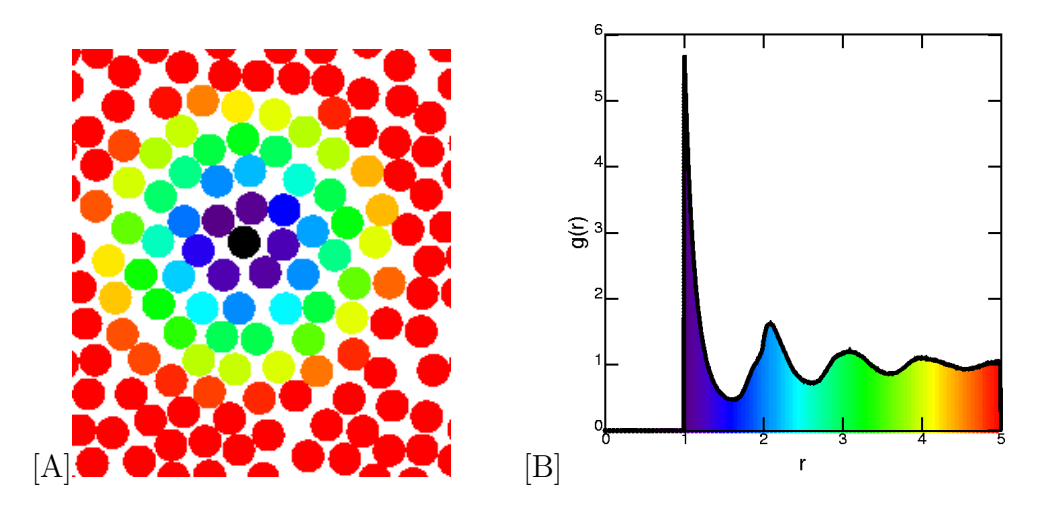


Figure 3.13: g(r) is computed for two-dimensional circles in the upper right image. Although the function is computed using all pairs of particles, I've emphasized one reference particle (black) in the left image to make it more obvious. According to the g(r) graph on the right, the neighbouring particles are shaded according to how far they are from the black particle.[29]

$$\rho = \frac{4\pi (\sigma/2)^3}{3} \frac{N}{V} \tag{3.1}$$

$$g(r) = \frac{V}{4\pi r^2 N^2} \left\langle \sum_{i} \sum_{i \neq j} \delta(r - r_{ij}) \right\rangle$$
 (3.2)

For Calculating in 3D:

- consider a particle and chose a value dr
- measures the number of particles between the sphere of radius r and the sphere of

radius dr+r

- then multiplies it by  $\frac{1}{4\pi r^2 dr}$  (1/volume of shell) and then divide it by number density, this will make sure that g(r) is 1 at large distances.
- loop it over other particles and divide it by the number of particles which are considered (which is usually total number of particles N)

For Calculating in 2D:

- consider a particle and chose a value dr
- $\bullet$  measures the number of particles between the circle of radius r and the circle of radius dr+r
- then multiplies it by  $\frac{1}{2\pi r dr}$  (1/volume of shell) and then divide it by number density, this will make sure that g(r) is 1 at large distances.
- loop it over other particles and divide it by the number of particles which are considered

If particles are hard spheres and closely packed, then the first peak of g(r) is at a distance of the diameter of particles.

### 3.5 MSD Mean Square Displacement:

The mean square displacement (MSD), which is computed as the ensemble average for N particles with  $x_t^i$  being the location of particle i at time t, is a metric for how far a particle's position deviates from a specific position over time.

$$MSD(\Delta t) = \langle |x(t + \Delta t) - x(t)|^2 \rangle$$
(3.3)

$$MSD(\Delta t) = \frac{1}{N} \sum_{i=1}^{N} |x^{i}(t + \Delta t) - x^{i}(t)|^{2}$$
(3.4)

Three areas are commonly seen in the mean square displacement (MSD) as a function of time: a ballistic zone, a plateau zone, and a diffusive zone. Particles travel within a cage made of nearby particles in the ballistic zone, also known as the " $\beta$ -relaxation," where the MSD rises linearly with time and a quadratic slope denotes the lack of particle interference. After some time, a plateau zone develops as a result of interference from nearby particles, which causes particles to move in a cage-rattling manner. The MSD exhibits linear dependency with time in the diffusive area, also known as  $\alpha$ -relaxation  $\langle r^2(t)\rangle \approx t$ , which suggests that more particles escape the cage and diffuse there. Due to particle collisions in the  $\alpha$ -relaxation, but motions are unhindered in  $\beta$ -relaxation, there is a variation in slope between the two zones. The particles diffusivity can be connected by the Einstein-Strokes equation  $D = \frac{k_B T}{6\pi\eta r}$  to viscocity $\eta$ , radius of particle r and temperature T. so slop of MSD in Log-Log plot with time will give 4 times diffusivity D.

#### 3.5.1 Average Local Strain and Non-affine Displacement

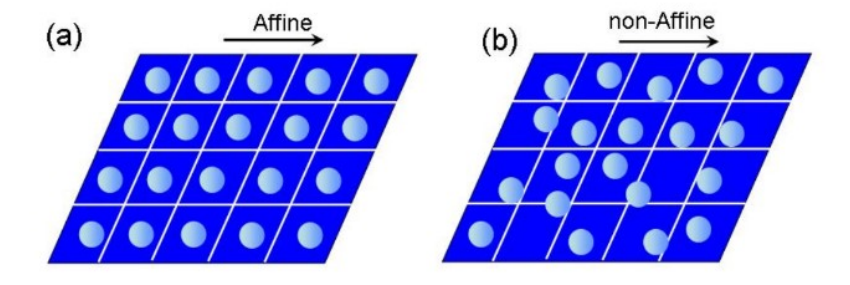


Figure 3.14: (a) is Affine deformation and (b) is Non-Affine Deformation[8]

If we apply pressure on a crystal from outside, its component particles experience a similar and equal strain with their adjacent particles, leading to a consistent deformation known as affine motion. Conversely, when external stress is applied to amorphous materials, the local strain experienced by their particles is uneven, resulting in non-affine displacement. Figure 3.14 depicts a very simplified depiction of affine and non-affine deformation In our study of colloidal glass, we will analyze both types of motion. Non-affine displacements[30] have a similar magnitude to relative affine displacements of adjacent particles and cannot be considered a minor correction. Disregarding them or treating them as a perturbation can

lead to highly unreliable estimations of macroscopic properties of materials such as elastic moduli. Therefore, non-affine displacements should not be overlooked in order to obtain accurate results in material science research.

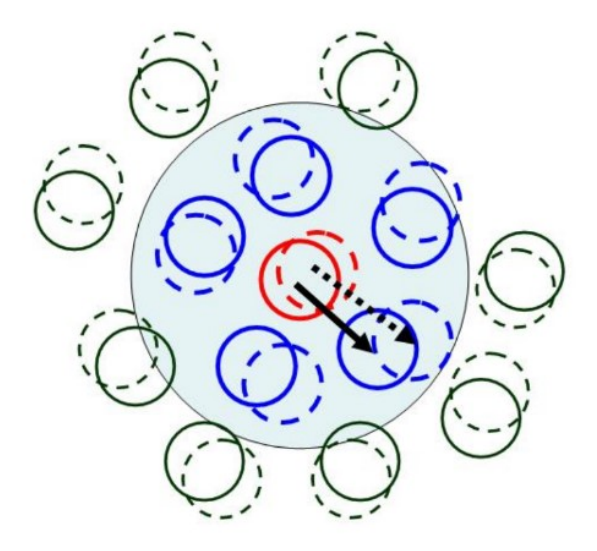


Figure 3.15: Determining the local stress at a specific location, The reference particles are represented by the colour red, and their neighbours are represented by the colour blue.[8]

To track the paths of particles, we identify the closest neighbours of each particle as those within a distance of  $r_0$ , which corresponds to the first minimum of the g(r) function. In figure 3.15 will explain this in 2D. The reference particle is depicted in red, while its neighbouring particles are illustrated in blue. The location of particles at time  $t - \Delta t$  and t are represented by thick and dotted lines, respectively. An affine transformation can be employed to explain the changes in closest neighbour vectors (arrow lines) during a time interval  $\Delta t$ . The optimal affine transformation  $\Gamma$  is chosen to minimize the quantity  $D^2$ , which is the mean-square difference between the actual displacements of neighbouring particles in relation to the central particle and the relative displacements they would have experienced if they were situated in a region of uniform deformation  $\Gamma$  [31].

$$D^{2}(t, \Delta t) = \sum_{n} \sum_{i} \left( r_{n}^{i}(t) - r_{0}^{i}(t) - \sum_{j} (\delta_{ij} + \Gamma_{ij}) \times [r_{n}^{j}(t - \Delta t) - r_{0}^{j}(t - \Delta t)] \right)^{2}$$
(3.5)

here the numbers i and j represent the spatial coordinates and n represents the number of particles that fall within the reference particle's interaction region, with n=0 serving as the reference particle. The  $i^{th}$  component of the  $n^{th}$  particle's location at time t is known as  $r_n^i(t)$ . Then, we identify the  $\epsilon_{ij}$  that minimises  $D^2$ .

$$X_{ij} = \sum_{n} [r_n^i(t) - r_0^i(t)] \times [r_n^j(t - \Delta t) - r_0^j(t - \Delta t)]$$
(3.6)

$$Y_{ij} = \sum_{n} [r_n^i(t - \Delta t) - r_0^i(t - \Delta t)] \times [r_n^j(t - \Delta t) - r_0^j(t - \Delta t)]$$
 (3.7)

$$\Gamma_{ij} = \sum_{k} X_{ik} Y_{ik}^{-1} - \delta_{ij} \tag{3.8}$$

The local departure from affine deformation or the non-affine deformation over the duration of the interval  $[t - \Delta t, t]$  is given by the minimized number of  $D^2(t, \Delta t)$  which is called  $D^2_{min}(t, \Delta t)$ . The symmetric portion of the deformation tensor yields the local strain tensor,  $\epsilon_{ij}$ .

$$\epsilon_{ij} = \frac{1}{2} (\Gamma_{ij} + \Gamma_{ij}^T) \tag{3.9}$$

The non-diagonal elements of strain tensor  $\epsilon_{ij}$  give shear parts of deformation, while its diagonal elements produce information on dilation components.

#### 3.5.2 Voronoi tessellation and Delaunay triangulation

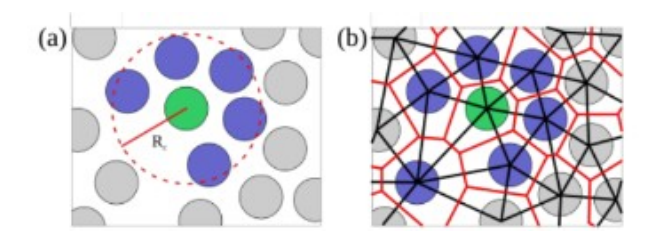


Figure 3.16: a)neighbours find based of distance and cutoff value b)lineas which are red are Voronoi tessellation and lines which are black are Delaunay triangulation

There are several applications for the computational geometry methods Voronoi tessellation and Delaunay triangulation. With the use of the Voronoi tessellation technique, a plane is divided into regions centered on a set of points, with each area including the points that are closest to that specific point. These areas are referred to as Voronoi cells, and the perpendicular bisectors of the connecting line segments between the nearby points serve as their borders. Delaunay triangulation is a technique for creating non-overlapping triangles from a group of points in a plane, ensuring that no point is inside the boundary of any triangle. Triangles formed using the Delaunay triangulation have the property that their minimum angles are all maximized, making them more stable and less prone to distortion. In disciplines including computer graphics, computer vision, geographic information systems (GIS), and simulation of physical processes, both Voronoi tessellation and Delaunay triangulation are often utilised.

#### 3.5.3 Traking of Particles

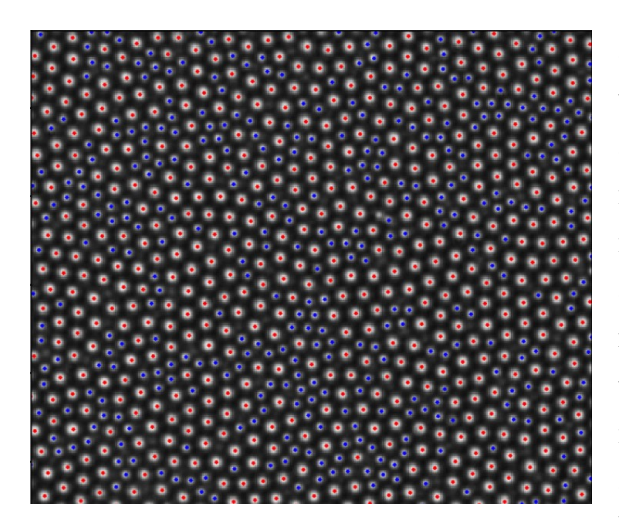


Figure 3.17: Overlap of tracked position by trackpy on the raw image. Red particles are 3.34  $\mu m$  and blue are 2.32  $\mu m$  respectively

The Trackpy algorithm is used for feature finding and particle tracking in 2D images. It is an extension of the Crocker and Grier algorithm [32] and returns particle information such as position. frame number, eccentricity, mass, and particle number from a set of ordered images. Before applying the algorithm, images are processed to remove geometric distortions, non-uniform contrast, and noise. The algorithm reads images and identifies bright particles on a dark background, and can also invert the image if necessary. The background is removed by calculating a boxcar average of intensities and subtracting it from the original image. Noise is reduced by convolving the image with a Gaussian surface half width  $\lambda n$  $\approx 1$  pixel. Particle positions are refined by finding local brightness maxima within a certain dis-

tance and calculating the brightness centroid. Suspicious particles are discarded. Trackpy

is used to track particles in a 2D. The modeling to background is done by average boxer intensity

$$A_{\omega}(x,y) = \frac{1}{(2\omega + 1)^2} \sum_{i,j=-\omega}^{\omega} A(x+i,y+j)$$

The boxcar average assigns the pixel brightness as an average of its neighbor's brightness, thereby smoothing the picture with a spectrum of w. And the formula yields the noise-reduced image:

$$A_{\lambda_n}(x,y) = \frac{\sum_{i,j=-\omega}^{\omega} A(x+i,y+j) exp(\frac{-i^2-J^2}{4\lambda_n^2})}{\sum_{i,j=-\omega}^{\omega} exp(\frac{-i^2-J^2}{4\lambda_n^2})}$$

The background is removed and the local intensity peak as the particle center is found to the accuracy of pixel(width=w) to sub-pixel accuracy is improved by figuring out the brightness centroid surrounding the local brightness maximum. By determining the offset from local maxima to the center of brightness for each particle, it is further improved.

$$\begin{pmatrix} \epsilon_x \\ \epsilon_y \end{pmatrix} = \frac{1}{I} \sum_{i^2 + j^2 < \omega^2} \begin{pmatrix} i \\ j \end{pmatrix} A(x+i, y+j)$$

I is integrated intensity. we use this algorithm to track the position of our colloidal and link the particles with an id and get the trajectory as it is the crucial step for the rest of the analysis. This data is taken at 10FPS for 500s the laser was on and the rest 500s laser was off.

# Chapter 4

# Results and Discussion

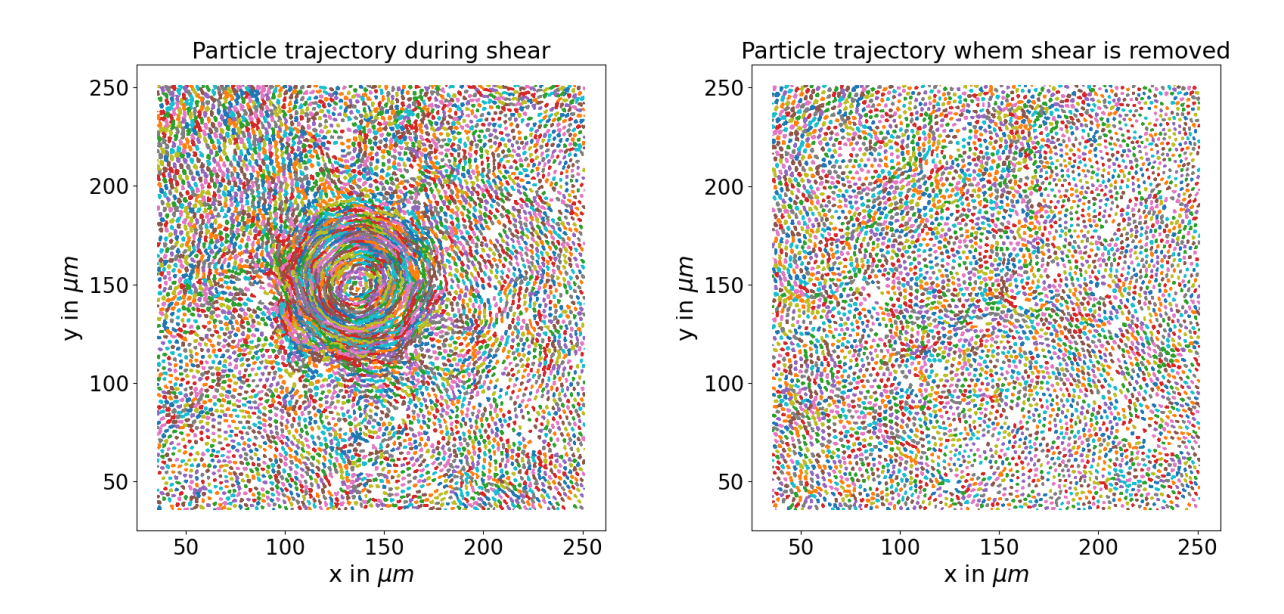


Figure 4.1: Tracked trajectory of all particles a)when Shear is applied(Laser On) For 500s b) after shear is removed (Laser Off) for remaining 500s

By utilizing the Cocker and Grier algorithm, as discussed in a previous section, we were able to determine the position of the particle with minimal subpixel biasing and track its trajectory. The algorithm accurately located the center of the particles, which overlapped with the raw data image and exhibited good alignment. To convert the pixel values to micron measurements, we rescaled them using the standard scale made by photo-lithography, where

1 pixel is equivalent to 0.28 microns. Figure 4.1 depicts the tracked trajectory of the particles after linking them and assigning each particle a unique reference ID. The trajectory is plotted after compensating for drift. The right figure illustrates the scenario where the laser was turned on for 500 seconds, while the left figure represents the scenario where the laser was turned off for the remaining 500 seconds.

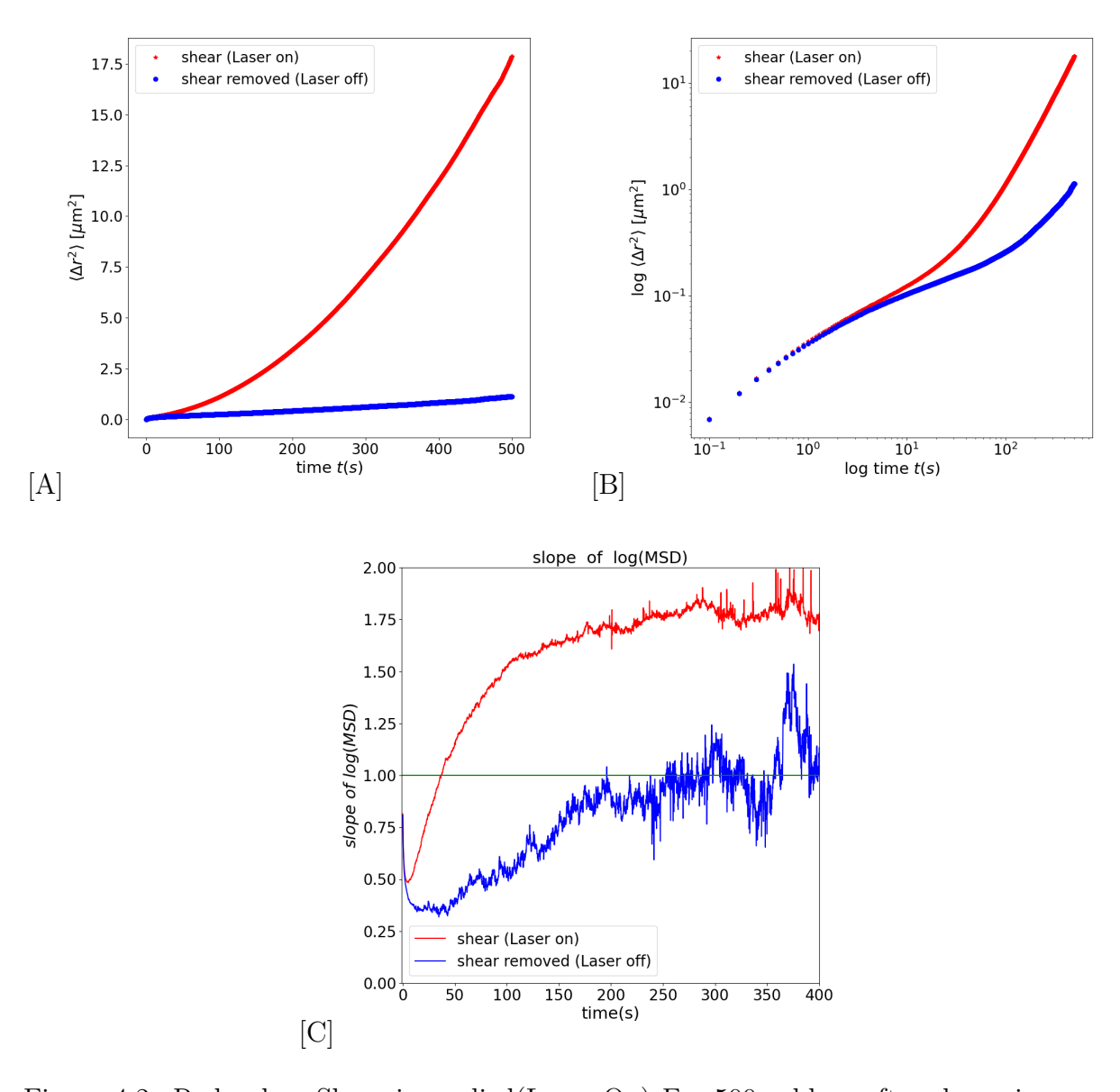


Figure 4.2: Red, when Shear is applied(Laser On) For 500s. blue, after shear, is removed (Laser Off) for the remaining 500s. a) MSD vs Time b) MSD vs Time In log-log Scale, c) slop of Log-Log MDS with time

The area fraction of the colloidal glass used in this study is 0.76. At this area fraction, the colloidal monolayer behaves as a glassy system in 2D. This is confirmed by the plateau observed in the mean square displacement (MSD) as shown in Figure 4.2, indicating the glassy nature of the system. Interestingly, the MSD of the shared particles is higher compared to when shear is removed. During shear, the system relaxes faster, and the slope of the MSD in the log-log plot is much higher. However, after shear removal, the slope of the MSD decreases, suggesting a plateau, and the relaxation occurs more slowly (over 250 seconds) compared to the sheared case where it decreases to less than one for short times and then relaxes at more than one slope, indicating the system is under the influence of shear, as captured by the MSD.

When examining the trajectories of particles in Figure 4.1, it was intriguing to observe that even though angular momentum from the LG Beam was applied only at the edge and limited to one particle diameter, the inner particles also exhibited rotation. To gain a better understanding, we analyzed the displacement field and calculated the angular velocity

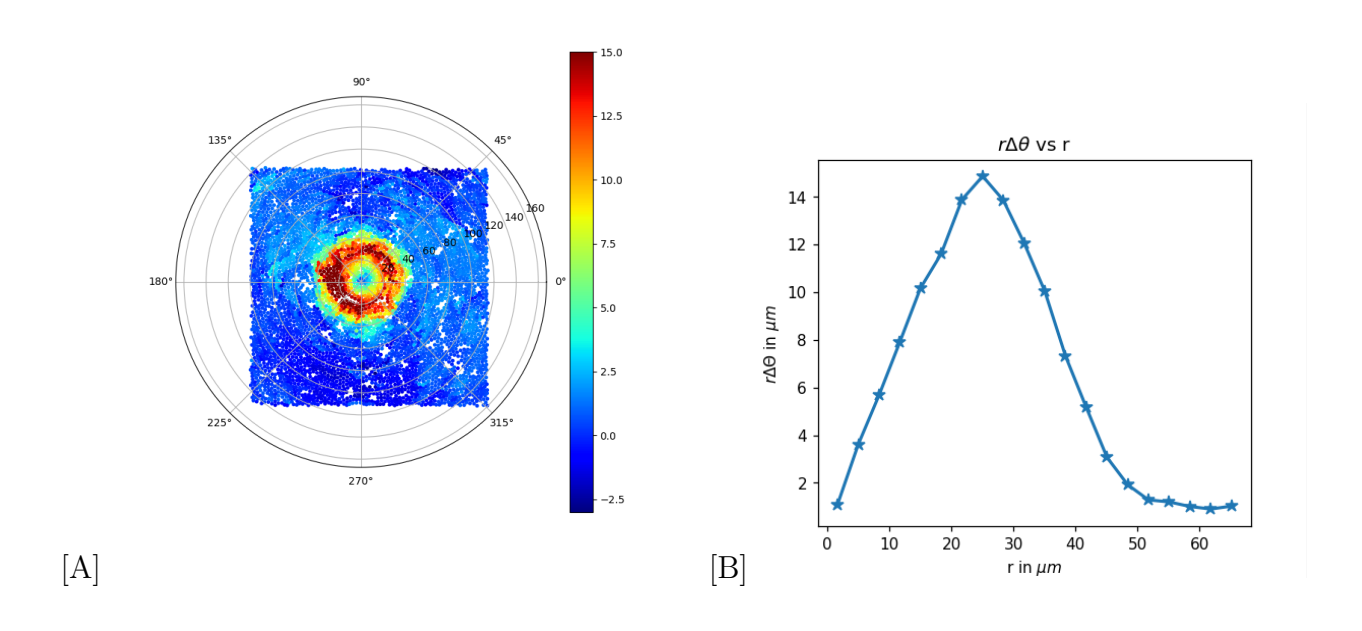


Figure 4.3: a)Displacement Profile plotted in polar coordinate b) Azimuthal average of Displacement  $(r\Delta\theta)$  from the center of shear circle

The displacement profile, as expected and shown in Figure 4.3, exhibits a maximum dis-

placement at the trapping ring, located approximately  $r_0 = 27\mu m$  away from the center of the Trapping Circle. This is depicted in the azimuthal average of the displacement profile with respect to the distance r from the center of the trap ring, shown in Figure 4.3 on the right. We use this distance to calculate the reference strain, which is given by  $strain = \frac{r_0 \Delta \theta}{L}$ , where L represents the distance from the trapping ring to the boundary of the experimental field of view. Therefore, with  $r_0$  and L fixed,  $\Delta \theta$ determines the value of the strain

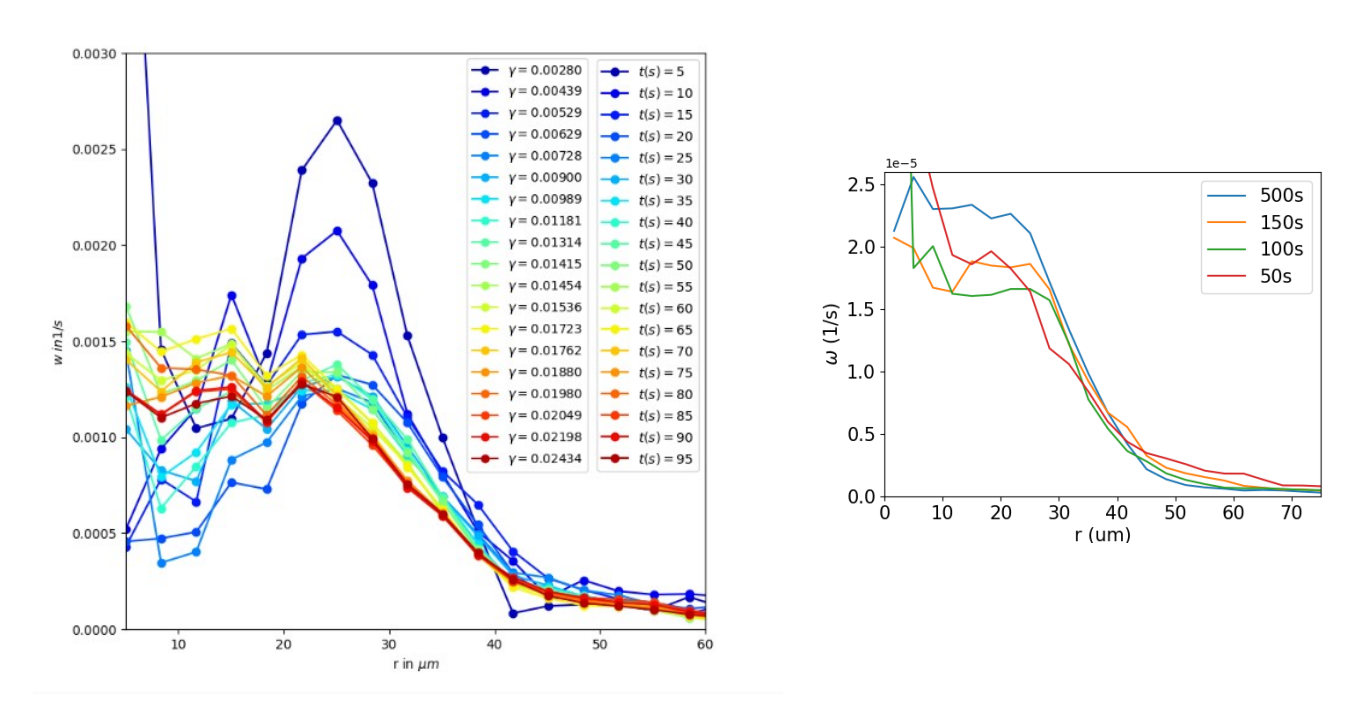


Figure 4.4: a)Angular velocity vs distance from trapping ring center, the color indicates time (blue to red) or strain b) at longer time the angular velocity will have a constant value for different amount of shear time datas

The figure 4.4 shows how the angular velocity of particles varies with distance, denoted as "r", from the center of the trap. The color indicates the time or amount of strain that has occurred over time. At the beginning of the shear, there is a peak at  $r_0$  that reduces, and the angular velocity of inner particles increases with time. When the laser is turned on, only the particles that get trapped acquire angular momentum and angular velocity. However, after approximately 20 to 30 seconds, the momentum starts to transfer towards the center of the trapping ring due to particle interactions. Inside the trapping ring, the angular velocity of particles starts to increase, and eventually converges, resulting in all particles inside the

trapping ring having the same angular velocity, causing them to rotate as a rigid body. Similar effects can be observed for different shear time data, as shown in the right plot of figure 4.4. However, there is a shear band[4] occurring between the distances of 30 to 45  $\mu m$  from the center.

To identify the location of defects in crystalline solids, we can structurally identify the defect, and under shear, these defects act as plastic carriers. Around these defects, there are more rearrangements of particles. However, in the case of amorphous solids, we apply similar logic to identify locations analogous to the defects in this system, by looking at regions with more rearrangements of particles.

 $D_{min}^2$  is a parameter that we discussed in an earlier section, and it is a very good parameter for identifying the locations of defects. It is calculated by subtracting affine displacement from real displacement to obtain non-affine displacement. We maximize the affine displacement part to obtain  $D_{min}^2$  for finding locations of defects, and we set a threshold value for  $D_{min}^2$  (in our case, it is  $2\mu m^2$  for the top 1.5% of particles) above which defects are identified. We then filter out only the local maxima of such  $D_{min}^2$  values above the threshold as our defects. We observe displacement between 200s, so that  $D_{min}^2$  will develop to find the calculation. The number of neighbours lost is also a parameter that gives similar regions for identifying locations. As we can see from Figure 4.5, both parameters match, confirming more rearrangements around areas with high  $D_{min}^2$  values.

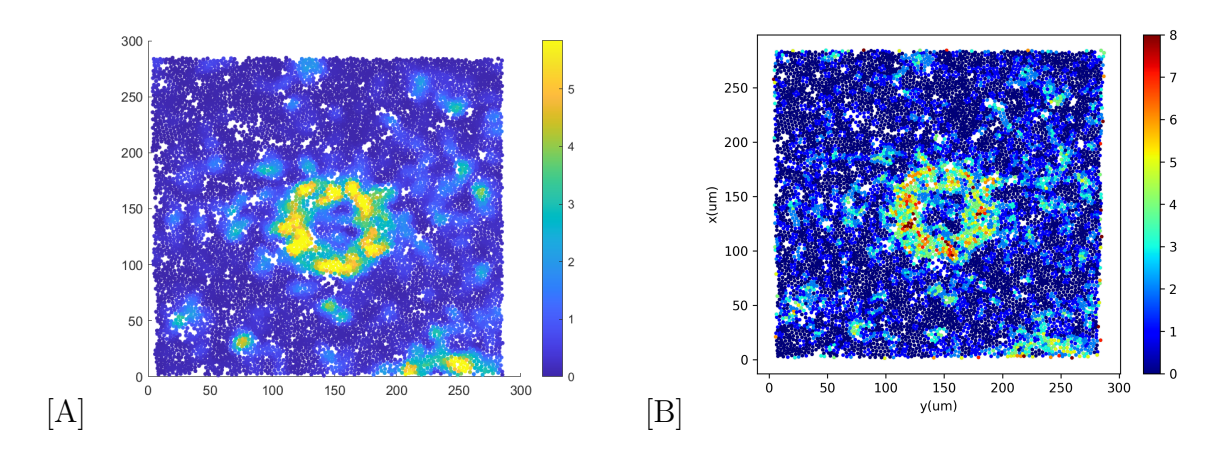


Figure 4.5: a) $D_{min}^2$  ( $\mu m^2$ ) b) Number of neighbours lost both are giving similar regions

For the above figure, calculations were done for a gap interval of 400s, but similarities were

found at all time scales. For further calculations, we used  $D_{min}^2$  because it is a continuous real number, whereas the number of neighbors lost is a discrete integer value. The number of neighbors lost is calculated by finding neighbors through Voronoi tessellation (Delaunay triangulation).

If we consider particles whose  $D_{min}^2$  is above the threshold value and is a local maximum, and look at the pair correlation function g(r) for these defect particles to obtain the radial distribution of particles averaged over these defects and over a 20s time period during shear.

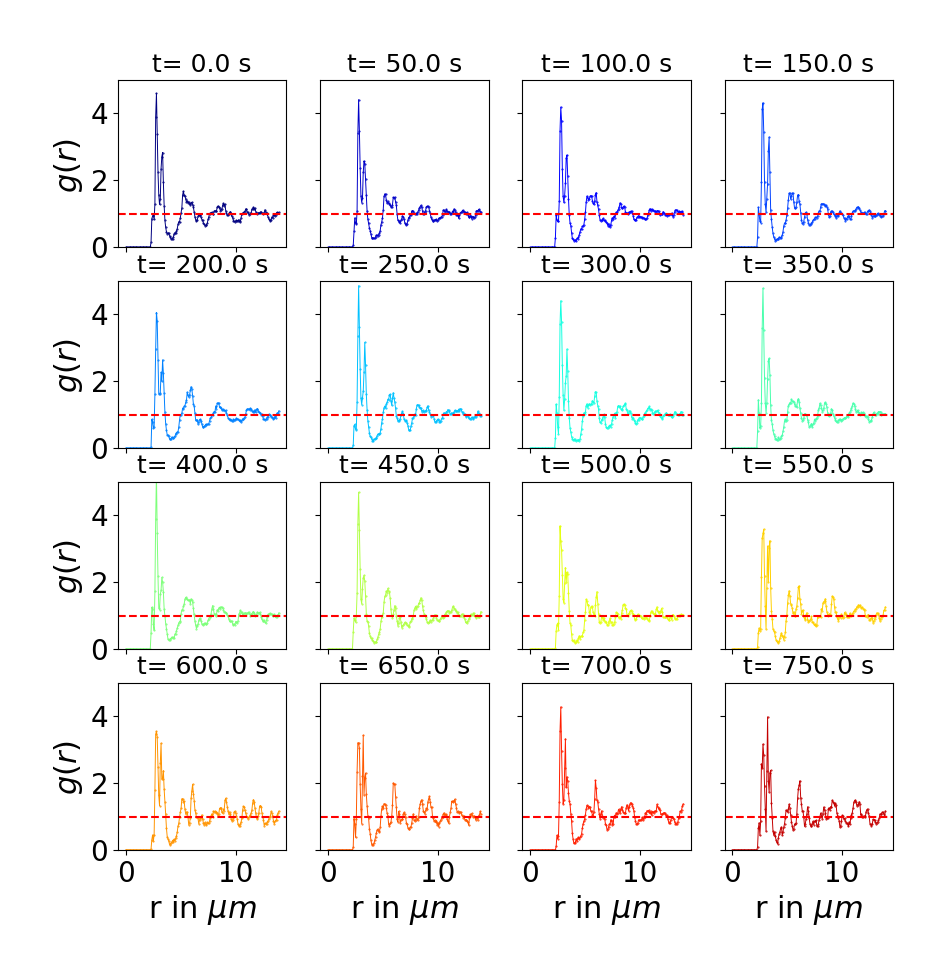


Figure 4.6: Radial distribution function for defect particles

There is a strong structural ordering of defects during shear, as evident from the pair correlation plot of defects shown in Figure 4.6. The function g(r) displays prominent peaks

at the diameter of small particles  $(2.32\mu m)$ , large particles  $(3.34\mu m)$ , and  $(2.83\mu m)$  during shear. However, even after shear is removed (after 500s), these peaks continue to persist for some time. As the system relaxes, the first peaks gradually diminish and structural order diminishes, but it shows a long-range correlation with more peaks at higher r, and it does not converge to one, with higher peaks getting more resolved. This information indicates that the structure around defects is different during shear compared to when shear is removed.

To understand the orientation of these defects with respect to the shear direction, we calculate the displacement field for each frame between 30 seconds. Then, we coarse-grain it by averaging the displacement of each particle's neighbours, as determined by Voronoi tessellation. Next, we examine the deformation vectors around these defect particles (based on the local maxima of  $D_{min}^2$  value), within a range of  $(3\sigma)$  3 times the diameter of the particle. We subtract the mean deformation vector for each defect (considered as an affine part) and observe the deviation from the mean to determine if the strain field is homogeneous. Interestingly, we observe that it is a heterogenous field, the radial component of these deformation vectors exhibits quadrupole symmetry[33], with two incoming and two outgoing vectors as seen in figure 4.7.

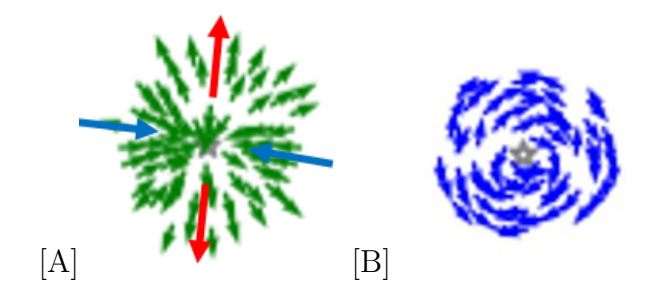


Figure 4.7: a) The radial component of the deformation vector has quadrupolar symmetry one direction particles are incoming and other direction particles are outgoing b) azimuthal component of the deformation vector

To determine the orientation of quadrupole symmetry defects, I considered only outgoing vectors and fitted an ellipse to the dumbbell-shaped outgoing vectors. By comparing the orientation of these ellipses with the shear direction (i.e., tangent to concentric circles from the center of the trapping ring), I observed that the defects were oriented at an angle of approximately 45 degrees from the shear direction during the application of shear. However, the orientation appeared random when the shear was removed. Figure 4.8 displays the locations of  $D_{min}^2$ , with stars marking the local maxima of  $D_{min}^2$  that exceed the threshold

value. These locations correspond to the defects present in our system. Figure 4.9 shows the radial component of the deviation of the displacement profile from the mean (approximately affine) displacement, indicating a quadrupole field. Figure 4.9 represents the azimuthal component of the displacement field around the locations of the defects identified in Fig 4.8.

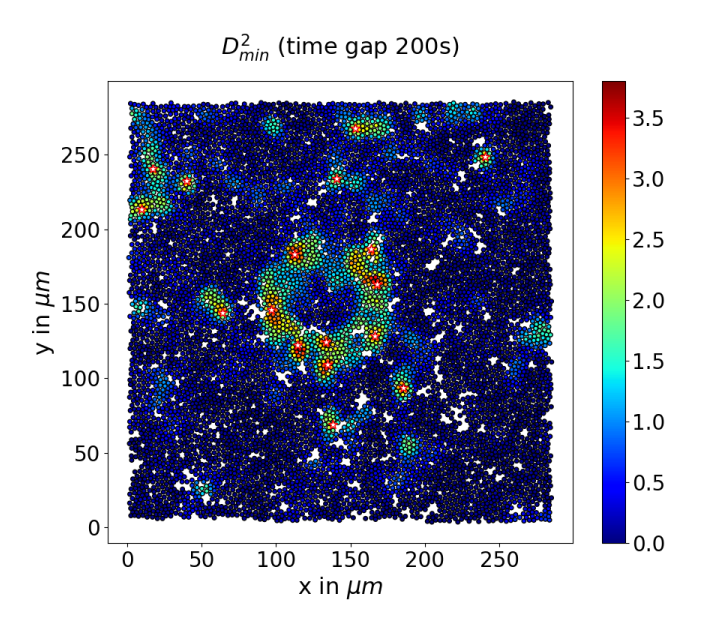


Figure 4.8: Defect Detected from maximums of  $D_{min}^2$ 

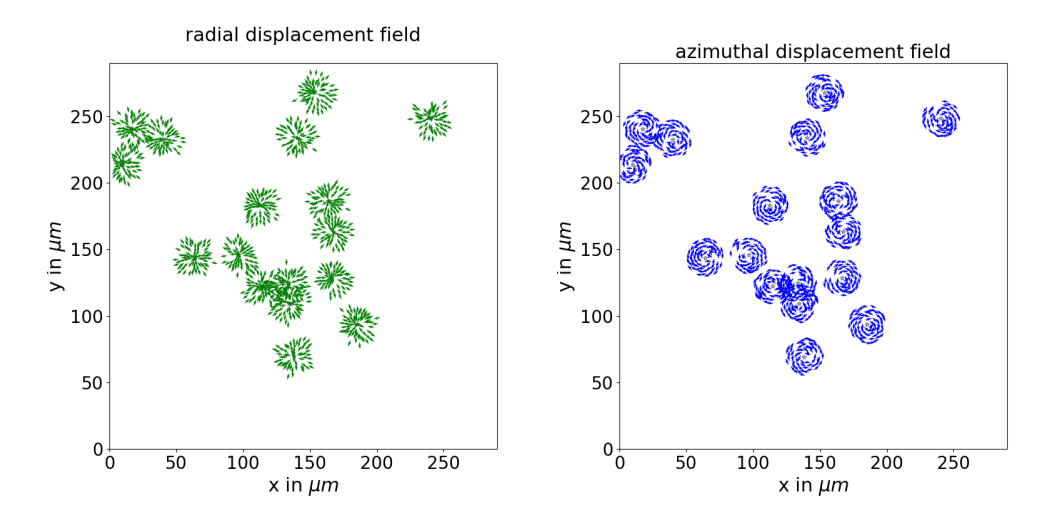


Figure 4.9: a)Radial component of the deformation vector has quadrupolar symmetry one direction particles are incoming and other direction particles are out going b) azimuthal component of the deformation vector

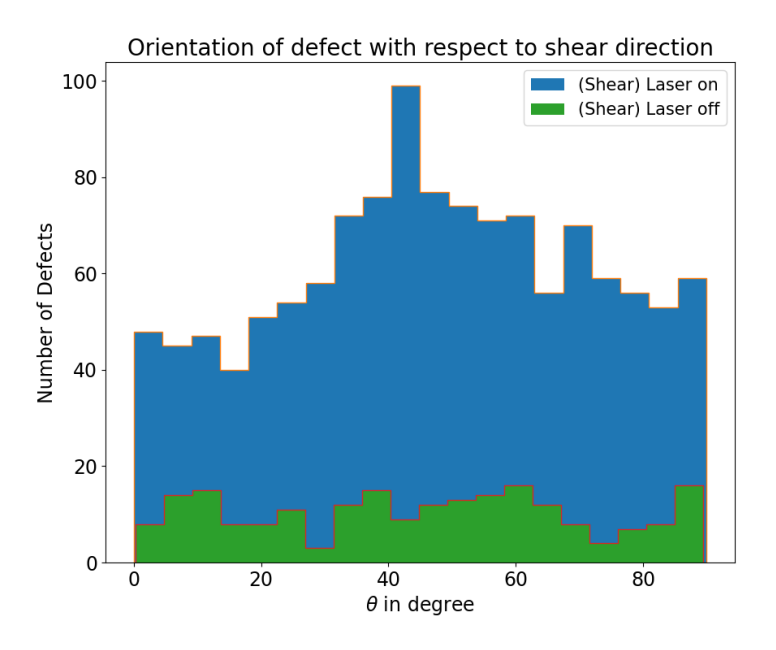


Figure 4.10: Orientation of defects with respect to shear direction

From Figure 4.10, it is evident that a clear peak is observed around 45 degrees when shear is applied, indicating that the defects tend to orient in a particular direction. However, when the shear is removed, the orientation appears to be random, as evidenced by the randomness in the peak when shear is removed.

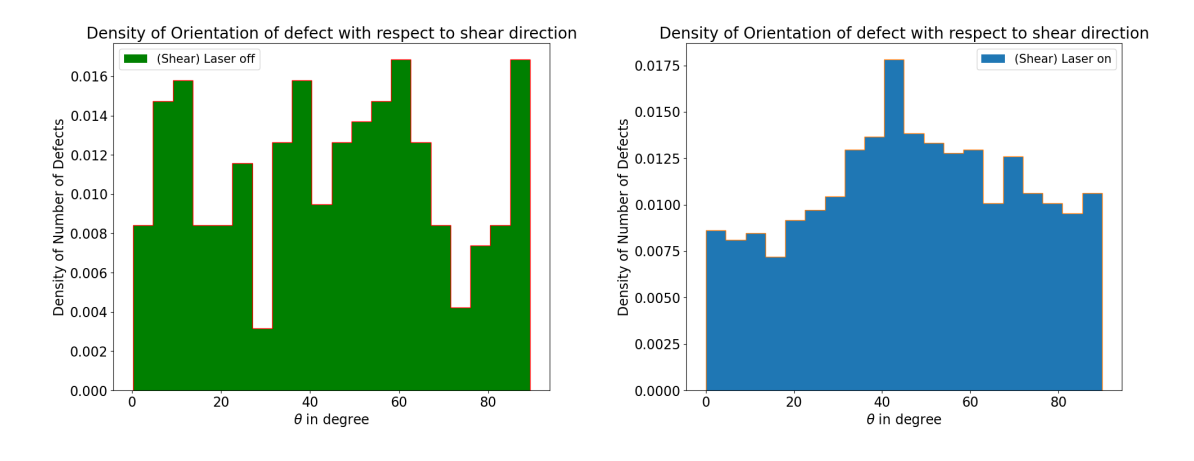


Figure 4.11: a)normalized density of orientation of defects when laser is off (no shear)b)normalized density of orientation of defects when laser is on (shear is on)

Figure 4.11 presents a normalized graph that provides the probability of defect orientation with respect to the sheared direction.

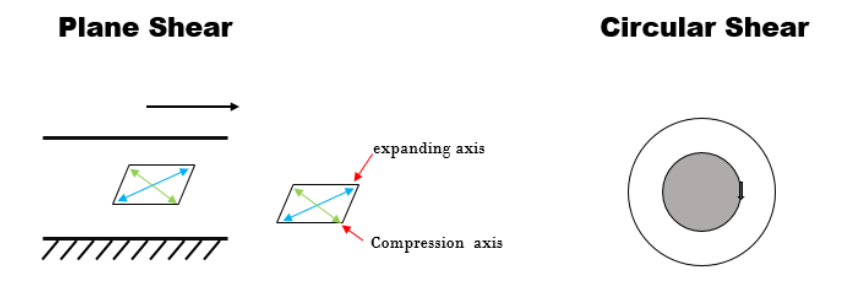


Figure 4.12: a) planer shear b) circular shear

The compression and extensional axes will form an angle of 45 degrees with the direction of shear, as depicted in figure 4.12. In this case, we are applying a circular shear. In circular geometry, we expect the defects to orient at 45 degree with respect to the direction of shear, which is the direction tangent to the circular region.

# Chapter 5

## Conclusion

In conclusion, our results demonstrate that the application of shear to a colloidal glass system using LG beam manipulation leads to interesting dynamics and rearrangements of particles. We successfully tracked the trajectories of particles using the Cocker and Grier algorithm, and found that the system exhibits glassy behaviour based on the plateau observed in the Mean Squared Displacement (MSD) analysis. The MSD is higher during shear, indicating faster relaxation of the system, and the slope of the MSD in the log-log plot is higher during shear, suggesting that the system is under drive.

We also observed that even though the shear was applied only at the edge of the system, inner particles also rotated, as confirmed by the displacement profile and angular velocity analysis. The angular velocity of particles varied with distance from the center of the trap, and after an initial peak, it converged to a constant value for particles inside the trapping ring, indicating rigid body rotation. However, a shear band was observed at a certain distance from the center, suggesting localized rearrangements of particles.

Furthermore, we utilized the  $D_{min}^2$  parameter to identify locations of defects in the amorphous solid, and found that regions with higher  $D_{min}^2$  values corresponded to areas of more particle rearrangements, analogous to defects in crystalline solids. Overall, our findings provide insights into the dynamics of colloidal glass systems under shear and shed light on the role of defects in the shear deformation and relaxation of amorphous systems. We also found out that there is a preferred orientation (45 degrees) of these defects with respect to the shear direction. Further studies can be conducted to investigate the effects of shear on dif-

ferent types of colloidal glasses and explore potential applications in materials science and engineering.

We also demonstrated the instrumentation of time-shared optical traps using AOD to have a large trapping field of around 150  $\mu m$  and 200 particles so that we can investigate the effect of random pinning of colloidal crystals on phonon mode.

#### 5.0.1 Future work

Till now the setup is optimized to have a larger field of trapping and tight single particle level trapping. Now we need to integrate the tracking of particle algorithm within LabVIEW and take data to understand the effect of random pinning of particles.

We are also taken data for oscillatory shear by changing the topological charge of Laguerre Gaussian beam as the optics path of alignment will not effect by changing the topological charge of Laguerre Gaussian beam. this is used to investigate how amorphous solids behave under oscillatory shear-like shear thickening and thinning will be investigated in future work. We are also interested in finding the relation between the structure and dynamics of these defects in amorphous solids.

We also further investigate how does orientation angle of these defects with respect to shear direction is effected by shear rate (Laser intensity). and how these defects will relax will be further studied.

# Bibliography

- [1] F. A. Lavergne, A. Curran, D. G. A. L. Aarts, and R. P. A. Dullens, "Dislocation-controlled formation and kinetics of grain boundary loops in two-dimensional crystals," *Proceedings of the National Academy of Sciences*, vol. 115, no. 27, pp. 6922–6927, 2018.
- [2] I. Buttinoni, J. Cha, W.-H. Lin, S. Job, C. Daraio, and L. Isa, "Direct observation of impact propagation and absorption in dense colloidal monolayers," *Proceedings of the National Academy of Sciences*, vol. 114, no. 46, pp. 12150–12155, 2017.
- [3] A. Nicolas, E. E. Ferrero, K. Martens, and J.-L. Barrat, "Deformation and flow of amorphous solids: Insights from elastoplastic models," *Rev. Mod. Phys.*, vol. 90, p. 045006, Dec 2018.
- [4] V. Chikkadi, D. M. Miedema, M. T. Dang, B. Nienhuis, and P. Schall, "Shear banding of colloidal glasses: Observation of a dynamic first-order transition," *Phys. Rev. Lett.*, vol. 113, p. 208301, Nov 2014.
- [5] P. Schall and M. van Hecke, "Shear bands in matter with granularity," *Annual Review of Fluid Mechanics*, vol. 42, pp. 67–88, 2010.
- [6] A. Argon, "Plastic deformation in metallic glasses," *Acta Metallurgica*, vol. 27, no. 1, pp. 47–58, 1979.
- [7] L. Berthier, G. Biroli, and J. Bouchaud, *Dynamical Heterogeneities in Glasses, Colloids, and Granular Media*. International Series of Monographs on Physics, OUP Oxford, 2011.
- [8] V. Chikkadi, "Source (or part of the following source): Type phd thesis title spatial correlations and deformation modes in sheared colloidal glasses," 2011.
- [9] F. Spaepen, "A microscopic mechanism for steady state inhomogeneous flow in metallic glasses," *Acta Metallurgica*, vol. 25, no. 4, pp. 407–415, 1977.
- [10] A. Argon, "Mechanisms of inelastic deformation in metallic glasses," *Journal of Physics and Chemistry of Solids*, vol. 43, no. 10, pp. 945–961, 1982.

- [11] J. D. Eshelby, "The elastic field outside an ellipsoidal inclusion," *Proceedings of the Royal Society of London. Series A. Mathematical and Physical Sciences*, vol. 252, no. 1271, pp. 561–569, 1959.
- [12] J. D. Eshelby, "The determination of the elastic field of an ellipsoidal inclusion, and related problems," *Proceedings of the royal society of London. Series A. Mathematical and physical sciences*, vol. 241, no. 1226, pp. 376–396, 1957.
- [13] P. Sollich, F. m. c. Lequeux, P. Hébraud, and M. E. Cates, "Rheology of soft glassy materials," *Phys. Rev. Lett.*, vol. 78, pp. 2020–2023, Mar 1997.
- [14] X. Li, Y. Zhou, Y. Cai, Y. Zhang, S. Yan, M. Li, R. Li, and B. Yao, "Generation of hybrid optical trap array by holographic optical tweezers," *Frontiers in Physics*, vol. 9, 2021.
- [15] D. Griffiths, *Introduction to Electrodynamics*. No. v. 2, Cambridge University Press, 2017.
- [16] B. Saleh and M. Teich, *Fundamentals of Photonics*. Wiley Series in Pure and Applied Optics, Wiley, 2019.
- [17] O. Émile, C. Brousseau, J. Émile, and K. Mahdjoubi, "Energy and angular momentum transfers from an electromagnetic wave to a copper ring in the uhf band," *Comptes Rendus Physique*, vol. 18, no. 2, pp. 137–143, 2017. Energy and radiosciences.
- [18] M. Nouri, Optical Orbital Angular Momentum Metrology. PhD thesis, 12 2014.
- [19] G. Volpe, O. M. Marago, H. Rubinsztein-Dunlop, G. Pesce, A. Stilgoe, G. Volpe, G. Tkachenko, V. G. Truong, S. Nic Chormaic, F. Kalantarifard, P. Elahi, M. Kall, A. Callegari, M. Marqués, A. Neves, W. L. Moreira, A. Fontes, C. L. Cesar, R. Saija, A. Saidi, P. Beck, J. Eismann, P. Banzer, T. Fernandes, F. Pedaci, W. Bowen, R. Vaipully, M. Lokesh, B. Roy, G. Thalhammer, M. Ritsch-Marte, L. Perez Garcia, A. Arzola, I. Perez Castillo, A. Argun, T. M. Muenker, B. E. Vos, P. Reece, F. Wang, D. McGloin, J. C. Ndukaife, R. Quidant, R. Roberts, C. Laplane, T. Volz, R. Gordon, D. Hanstorp, J. Marmolejo, K. Dholakia, G. Bruce, T. Li, O. Brzobohaty, S. H. Simpson, P. Zemanek, F. Ritort, Y. Roichman, V. Bobkova, R. Wittkowski, C. Denz, T. Betz, I. Cristiani, P. Minzioni, G. V. P. Kumar, A. Foti, M. G. Donato, P. Gucciardi, L. Gardini, G. Bianchi, A. Kashchuk, M. Capitanio, L. Paterson, P. Jones, K. Berg-Sorensen, Y. Barooji, L. B. Oddershede, P. Pouladian, D. Preece, C. Beck Adiels, A. C. De Luca, A. Magazzù, D. Bronte Ciriza, M. A. Iatì, and G. A. Swartzlander, "Roadmap for optical tweezers 2023," Journal of Physics: Photonics, 2023.
- [20] M. David, "Optical tweezers: 20 years on," Phil. Trans. R. Soc. A.3643521–3537 http://doi.org/10.1098/rsta.2006.1891, 2006.

- [21] A. Ashkin, "Arthur ashkin nobel lecture. nobelprize.org. nobel prize." https://www.nobelprize.org/prizes/physics/2018/ashkin/lecture/¿, 2018. Accessed on 2022-10-31.
- [22] A. Ashkin, J. M. Dziedzic, J. E. Bjorkholm, and S. Chu, "Observation of a single-beam gradient force optical trap for dielectric particles," *Optics letters*, vol. 11, no. 5, pp. 288–290, 1986.
- [23] G. Spalding, J. Courtial, and R. Leonardo, *Holographic Optical Tweezers*, pp. 139–168. 12 2008.
- [24] I. I. S. Gabriel L. Stockdale, "The design and construction of a holographic optical trap based on a liquid crystal spatial light modulator." https://www.colorado.edu/physics-jila-reu/sites/default/files/attached-files/stockdale\_orbital\_dynamics\_of\_the\_laser\_interferometer\_space\_antenna.pdf, 2008.
- [25] D. K. Gupta, B. V. R. Tata, and T. R. Ravindran, "Optimization of a spatial light modulator driven by digital video interface graphics to generate holographic optical traps," *Appl. Opt.*, vol. 57, pp. 8374–8384, Oct 2018.
- [26] P. Jones, O. Marag, and G. Volpe, *Optical Tweezers: Principles and Applications*. Cambridge University Press, 2015.
- [27] Z. Zhao, "High precision optical wavefront generation using liquid crystal spatial light modulator (lc-slm)," in *Liquid Crystals* (P. K. Choudhury and A.-B. M. Ibrahim, eds.), ch. 5, Rijeka: IntechOpen, 2021.
- [28] G. S. Shashank, "Dynamics of glass-forming liquids and shear-induced grain growth in dense colloidal suspensions." https://etd.iisc.ac.in/handle/2005/3730, 2015.
- [29] E. Weeks, "pair correlation function." https://physics.emory.edu/faculty/weeks/idl/gofr.html.
- [30] V. Chikkadi and P. Schall, "Nonaffine measures of particle displacements in sheared colloidal glasses," *Phys. Rev. E*, vol. 85, p. 031402, Mar 2012.
- [31] M. L. Falk and J. S. Langer, "Dynamics of viscoplastic deformation in amorphous solids," *Phys. Rev. E*, vol. 57, pp. 7192–7205, Jun 1998.
- [32] J. C. Crocker and D. G. Grier, "Methods of digital video microscopy for colloidal studies," *Journal of colloid and interface science*, vol. 179, no. 1, pp. 298–310, 1996.
- [33] V. Chikkadi, G. Wegdam, D. Bonn, B. Nienhuis, and P. Schall, "Long-range strain correlations in sheared colloidal glasses," *Phys. Rev. Lett.*, vol. 107, p. 198303, Nov 2011.